PHYSICAL REVIEW B VOLUME 16, NUMBER 1 1 JULY 1977

# Ultrafast transient response of solid-state plasmas. I. Germanium, theory, and experiment*

Ahmet Elci and Marlan O. Scully
*Department of Physics and Optical Sciences Center, University of Arizona, Tucson, Arizona 85721*

Arthur L. Smirl
*Department of Physics, North Texas State University, Denton, Texas 76203*

John C. Matter
*Sandia Laboratories, Albuquerque, New Mexico 87115*

(Received 7 June 1976)

A first-principles theory is developed for the generation and the subsequent transient behavior of dense electron-hole plasmas produced in germanium by intense picosecond optical pulses. Experimental data are discussed and compared with the theory. It is shown that the valley structure of the Ge conduction band, phonons, and plasmons play significant roles in the generation and the temporal evolution of the plasma. The agreement between the theory and experiments is good. Some predictions of the theory are discussed.

## I. INTRODUCTION

The development of mode-locked lasers[1] that produce optical pulses of a few picoseconds duration and peak powers of $\gtrsim 10^9$ W has made possible recent experimental investigations of ultrafast electronic processes in semiconductors.[2-5] In these experiments, the general method is to subject an intrinsic semiconductor first to an intense picosecond (excitation) pulse[2] of frequency $\omega_0$ such that $\hbar\omega_0$ is greater than the band-gap energy of the material and to measure its transmission; then after some delay, to subject the same sample to a second (probe) pulse of the same frequency but lower intensity and measure its transmission. The transmission properties of the semiconductor are significantly altered when the excitation pulse creates a large free-carrier density, and the transmission of the probe pulse yields information concerning the temporal evolution of the free-carrier distribution. The ultrashort duration of the laser pulses makes it possible to follow this temporal evolution on a picosecond time scale.

In this paper we present a first-principles, theoretical treatment accounting for the observed behavior in the excitation and probe pulse measurements in terms of the energy-band structure and other well-known parameters of germanium (Ge). We note at the outset, however, that only certain of the myriad of possible electronic interactions are included in the present work. Future papers in this series will deal with other possible electron processes such as diffusion and Kane-like excitations.

In the remainder of this introductory section, we briefly review the experimental method and results (Sec. I A), summarize the pertinent germanium energy-band structure (Sec. I B), and qualitatively discuss the physical processes which occur during and after the nonlinear light absorption by germanium (Sec. I C). We expound on the theory in Sec. II. This elaboration proceeds through a discussion of electron-hole distributions (Sec. II A), direct absorption (Sec. II B), free-carrier absorption (Sec. II C), phonon-assisted relaxation (Sec. II D), plasmon-assisted recombination (Sec. II E), rate equations for absorption and transmission (Sec. II F), and integration of the dynamical equations (Sec. II G). The final section (Sec. III) of the main text contains the comparison of theory with experiment and our conclusions. Several appendixes include detailed calculations which allow us to make critical simplifying assumptions in our theoretical model. Appendix A considers intervalley transitions via phonon emission; Appendix B discusses Coulomb thermalization; Appendix C derives radiation absorption rates; Appendix D expands on phonon-assisted relaxation. Finally, in Appendix E, we present some details concerning the experimental method and apparatus.

### A. Experimental method and data

A mode-locked Nd:glass ($\hbar\omega_0 = 1.17$ eV) laser produces a train of pulses; each pulse is typically 5–10 psec in duration and has $\sim 10^{15}$ quanta. Using a laser-triggered spark gap and electro-optical shutter, a single pulse can be isolated from this train of pulses.[6]

In the first experiment, this single pulse is passed through a variable attenuator and focused on an intrinsic 5.2-$\mu$m-thick Ge sample [Fig. 1(a)]. The focused spot is approximately 250 $\mu$m in diameter. The transmission of this pulse is then mon-

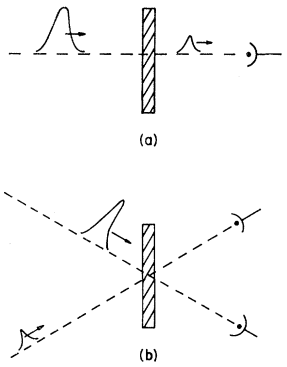


FIG. 1. Schematic diagram of picosecond experiments for (a) saturation and (b) excitation pulse/probe studies.

itored. The transmission data as a function of incident number of quanta, for two initial sample temperatures (77 and 297 °K), are shown in Fig. 2. At low pulse energies, transmission follows Beer's law.[7] As the incident number of quanta increases, transmission increases and eventually saturates. Near $5 \times 10^{14}$ quanta samples are damaged.

In the second experiment [Fig. 1(b)], the sample is first irradiated by an excitation pulse of sufficient energy to cause enhanced transmission. It is then followed, at a later time $t_d$, by a probe pulse which is about 5% as intense as the excitation pulse. The excitation and probe pulses are derived from a single pulse as described in Appendix E. Probe pulse transmission data versus delay time $t_d$ are shown in Fig. 3 for initial sample temperatures of 77 and 297 °K and for a fixed excitation pulse of about $10^{14}$ quanta. There is a sharp increase in transmission, a spike, in the region of temporal coincidence of the probe and excitation pulses (at $t_d = 0$). The spike is due to the scattering of the excitation pulse into the probe pulse by an index grating formed by the interference of these two coherent pulses in the crystal.[4,8] In this paper,

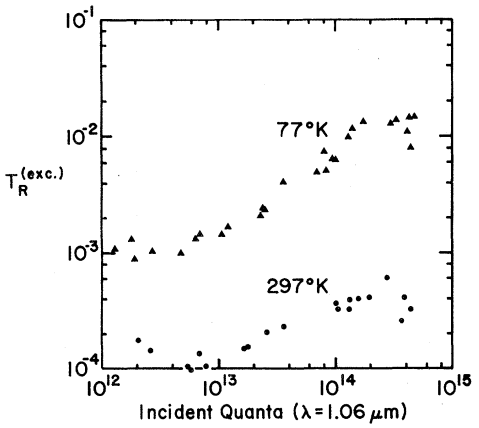


FIG. 2. Excitation pulse transmission (saturation) data.

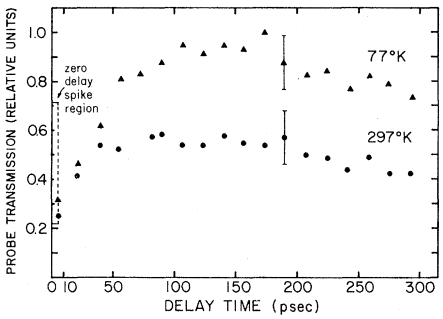


FIG. 3. Probe pulse transmission data. Relative transmission units are given by the ratios of the excitation transmission to probe transmission for each delay, normalized such that the peak of the 77 °K curve is unity.

we will be concerned with the probe transmissions at delay times longer than the pulse width. In this region, probe transmission increases relatively rapidly, reaching a maximum near $t_d \sim 100$ psec, thereafter decreasing slowly. Figure 4 shows the probe pulse data for different excitation pulse intensities and for an initial sample temperature of 77 °K. Ratios labeling these curves are the normalized relative transmissions of excitation pulse to probe pulse. The details of the experiments are further discussed in Appendix E.

### B. Review of Ge energy structure

The energy-band structure of Ge is well known,[9] and is shown in Fig. 5. The significant features of the conduction band are the locations of the conduction-band valleys. The minima of these valleys are quite close in energy. The minimum located at Γ is separated from the top of the valence band by 0.805 eV at 300 °K. This separation is 0.889 eV at 77 °K. The indirect gap located at $L$ has a separation of 0.664 eV at 300 °K and a separation of 0.734 eV at 77 °K. The band minimum located near $X$ is 0.18 eV higher than the minimum at $L$. There are three other valleys such as the one in the [111]

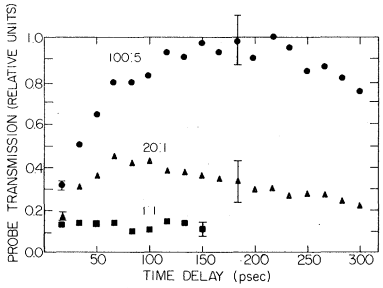


FIG. 4. Probe pulse transmission data for different excitation pulse intensities.

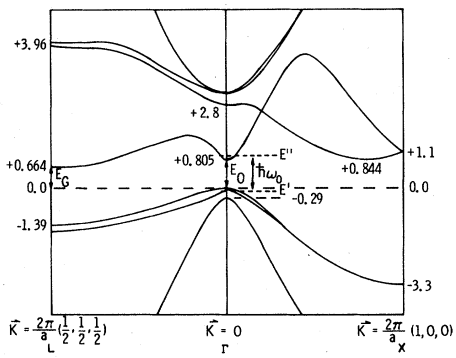


FIG. 5. Ge energy-band (eV) structure at 300 °K.

direction whose minima are located exactly at the Brillouin-zone boundary. There are five other valleys like the one in the [100] direction.[10] The constant energy surfaces in these valleys are elongated ellipsoids. The density-of-states effective mass[11] for the $L$ valleys is $m_c \simeq 0.22m$.[9] The density-of-states effective mass of the central conduction-band valley is taken to be[9] $m_0 \simeq 0.1m$ at 300 °K and $0.04m$ at 77 °K.

The valence band maximum is at Γ. Two of the valence bands, which are degenerate throughout the Brillouin zone when spin-orbit coupling is neglected, we call heavy-hole bands, while the third is termed the light-hole band. At Γ, the light-hole band is lowered by spin-orbit coupling with respect to the heavy-hole bands by about 0.28 eV. Except for a small region near the center of the Brillouin zone, the structure introduced by the spin-orbit coupling in the heavy-hole bands is relatively minor. We will treat the two heavy-hole bands as degenerate. The effective mass of the two heavy-hole bands in the central region of the Brillouin zone is $m_h = 0.34m$.[9] We will ignore the light-hole band owing to its small contribution to the hole density of states and its large separation from the Γ conduction-band edge, which makes its contribution to light absorption negligible in the current experiments.

Let us remark that an enormous simplification results in the algebra of the subsequent sections if we treat $L$ and $X$ valleys in an equivalent manner and assume parabolic energy bands with the effective masses mentioned above. The quantitative results are not affected much by such an approximation because these valleys enter into the absorption properties mainly through their density of states. This approximation results in the simplified band structure shown in Fig. 6, in which the four "effective" $L$ valleys and six $X$ valleys are replaced by ten equivalent parabolic valleys. In each of these new valleys the effective mass for electrons is $m_c = 0.22m$. These ten equivalent valleys are at some indirect energy gap $E_G$, which is some average of the actual indirect gaps $E_L$ (at $L$) and $E_X$ (near $X$). The average we use is $E_G = \frac{1}{14}(8E_L + 6E_X)$. The new valleys are assumed to be centered in the Brillouin-zone boundaries. In this approximate band model, the Γ valley and the two degenerate valence bands are also taken as parabolic, with the effective masses $m_0 = 0.1m$ and $m_h = 0.34m$, respectively.

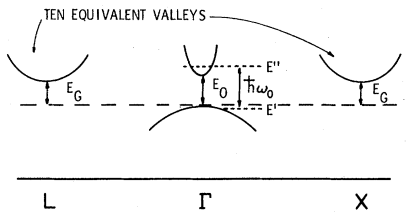


FIG. 6. Reduced Ge energy-band structure.

### C. Physics of nonlinear light absorption in Ge

When an excitation pulse is incident on a Ge sample, a portion is reflected. The unreflected portion of the excitation pulse enters the bulk of the crystal where most of it is absorbed. The light entering the bulk of the crystal is absorbed primarily by two processes. In the first process, "direct optical absorption," a quanta of light from the excitation pulse is absorbed by an electron which makes a transition from near the top of the valence band to the conduction-band valley near Γ, leaving behind a hole in the valence band. Such a process is allowed since the energy of the light quanta $\hbar\omega_0$ is greater than the direct band gap $E_0$. Once there are electrons in the conduction band and holes in the valence band, "free-carrier absorption" is possible. Free-carrier absorption is the process whereby an electron in any of the conduction-band valleys makes a transition to a state higher in that same valley by means of the simultaneous absorption of a quanta of light and the absorption or emission of a phonon (optical or acoustical). An identical process occurs for holes in the valence band. The rate for direct absorption is usually larger than that for free-carrier absorption; however, the rate at which direct absorption events can occur decreases as the number of occupied electron states in the Γ valley increases. On the other hand, the rate for free-carrier absorption events increases as the number of electrons (holes) in the conduction (valence) band increases.

Indirect phonon-assisted interband absorption processes, which involve the transition of an electron from the valence band near Γ to either the $L$ or $X$ conduction-band valleys by the simultaneous

absorption of a photon and the absorption or emission of a phonon, are not important in our problem. The probability that an electron will reach the $L$ or $X$ valley by means of a real optical transition to the $\Gamma$ valley followed by a phonon-assisted scattering to one of these side valleys is much greater than the probability that the electron will reach the same valley by means of a second-order phonon-assisted transition. For this reason, indirect optical-absorption events may be ignored.[12]

Because of the small number of electron states available in the $\Gamma$ valley, one might conclude that the direct transitions are saturated at relatively low pulse energies. In fact, this is not the case since an electron in the $\Gamma$ valley will rapidly emit or absorb a phonon and make a transition to one of the valleys at $X$ or $L$. A rate calculation in Appendix A shows that the rate for electron transitions from the $\Gamma$ valley to the $L$ valley is greater than $10^{14}$ sec$^{-1}$ since $\hbar\omega_0 > E_{L,X} + \max(\hbar\Omega_{\mu q})$ and since the electron-phonon coupling constants in Ge are relatively large. Here $E_{L,X}$ refers to the indirect gaps and $\Omega_{\mu q}$ to the phonon frequency of mode $\mu$ and momentum $\hbar\vec{q}$. Thus electrons are emptied from the central valley to the side valleys at a rate that is larger than the direct absorption rate, and any decrease in the number of states available for direct absorption is ultimately determined by the buildup of the electron populations in the $X$ and $L$ valleys.

Owing to the narrow bandwidth of the excitation pulse, only narrow regions of states in the central valley of the conduction and valence bands are optically coupled by direct transitions. Thus nonequilibrium carriers might be thought to occupy very localized regions within the conduction bands and valence band, respectively. However, because each carrier moves in the screened Coulomb field of the other carriers, carrier-carrier scattering events will occur. These events include electron-electron, electron-hole, and hole-hole collisions. The rate for such events is large. These collisions ensure that the electron and hole distributions will be Fermi-like. They also ensure that the Fermi distribution for holes and the Fermi distribution for the electrons will reach a common temperature which is in general different from the lattice temperature. Rate calculations in Appendix B using two non-Fermi-like distributions indicate that if they are not Fermi-like, their lifetimes are quite short compared to the inverse of the direct optical-absorption rate. For this reason we take the electron and hole carrier distributions to be Fermi-like at all times.

Electrons located high in a conduction-band valley may relax within that valley by phonon emission. Holes, of course, may also relax by emitting phonons. The effect of this relaxation is to reduce the electron temperature and increase the lattice temperature. The increase in lattice temperature due to these phonon-assisted intraband relaxation processes is significant only at very large pulse energies.

It is important to notice that the total number of carriers is unchanged by free-carrier absorption or phonon-assisted relaxation within the valleys. These processes serve only to elevate or reduce, respectively, the distribution temperature. Only direct absorption will increase the number of carriers. Recombination processes serve to reduce the carrier number.

The recombination processes can be divided into two general categories: radiative and nonradiative. In the present work, nonradiative recombination is much more important in reducing the carrier number than radiative recombination. As the carrier density builds up (as a result of direct absorptions) the plasma frequency of these carriers increases. At sufficiently large plasma frequencies, an electron in the $\Gamma$ valley can recombine with a hole near the top of the valence bands via emission of a plasmon. Normally, electrons near the conduction-band edge (at $\Gamma$) can recombine with holes via emission of plasmons only if the plasma frequency $\omega_p$ is larger than the direct gap frequency $E_0/\hbar$ [see Eq. (53)]. However, in our case, the plasma resonance is considerably broadened due to the nature of the direct absorption and subsequent scatterings between and within the $\Gamma$ valley and the $L$-$X$ valleys. Therefore, plasmon-assisted recombinations can occur at plasma frequencies lower than $E_0/\hbar$. As the electron and hole populations build up, the plasmon-assisted recombination rate becomes comparable to the direct absorption rate, causing the carrier number to saturate at plasma frequencies much less than $E_0/\hbar$. These plasmon-assisted recombinations can be as important in determining the final number of conduction electrons as the saturation in the total number of available electron states in the conduction band due to the buildup of the electron population.

The collective plasma oscillations have a lifetime that is short compared to a picosecond. The energy lost in the decay of the plasma oscillations is rapidly transferred to single electron and hole states and, thus, ultimately increases the temperature of the carrier distribution. Thus the plasmon-assisted recombinations both limit the number of carriers and raise the electron-hole temperature.

Radiative recombination may be of two types: direct or indirect. The recombination of an electron in the $\Gamma$ valley of the conduction band with a hole in the valence band by means of emission of

a photon is termed direct; the recombination of an electron in the $L$ or $X$ valley with a hole in the valence band by means of simultaneous emission of a photon and emission (or absorption) of a phonon is termed indirect. Both processes occur on time scales larger than nanosecond, and are not important in our problem.

The diffusion[4] of carriers from the interaction region (focused spot size times sample thickness) also reduces the carrier number. Preliminary diffusion (Boltzmann equation) calculations (to be published) indicate that the number of carriers leaving the interaction region on a picosecond time scale is small. In any case we are able to account for our experimental results without invoking diffusion.

In summary, the following rapid processes are invoked in explaining the passage of our 1.06-$\mu m$ psec pulses through Ge: particle-particle scattering, electron-phonon scattering, direct and free-carrier absorption, and plasmon-assisted interband electron-hole recombinations. In the calculation, radiative recombination and diffusion are ignored as discussed above.

Physically, the single pulse transmission of Ge as a function of incident pulse energy (see Fig. 2) can be accounted for by direct interband transitions followed by heating of the electron distribution as follows: When the excitation pulse enters the crystal, it is absorbed by direct optical transitions, creating a large number of electrons in the central valley of the conduction band. These electrons are quickly scattered to the side valleys by phonons. Particle-particle scattering events ensure that the carrier distributions are Fermi-like and that both electron and hole distributions have the same temperature. The transmission initially rises due to the saturation of the available optically coupled states as a result of direct absorption. Further increase in the transmission for intensities larger than $10^{14}$ quanta is hindered as the electrons are heated and removed from these states by free-carrier absorption and plasmon-assisted recombination. For these excitation pulse intensities, electrons in the $\Gamma$ valley fall to the hole pockets in the valence bands via plasmon emissions at a rate comparable to light absorption thus limiting the carrier density.

After the passage of the excitation pulse, the interaction region of the sample contains a large number of carriers with a high electron-hole temperature. Plasmon-assisted recombinations are essentially turned off when the excitation pulse has passed. This is discussed in detail in Sec. II E. As time progresses, the distribution temperature is reduced by phonon-assisted intraband and intravalley relaxation; the probe pulse interrogates this evolution of the distribution, since it is a sensitive measure of whether the optically coupled states are available for absorption or are occupied.

The probe pulse transmission (see Fig. 3) can be understood in the following way. After the passage of the excitation pulse, the electrons (holes) are located high (low) in the valleys because of the high distribution temperature, leaving the states that are optically coupled available for absorption. Hence probe transmission is small. Later, as the distribution cools by means of intraband phonon-assisted transitions and carriers fill the states needed for absorption, the probe transmission increases. Finally, as the distribution temperature cools to near the lattice temperature, the electrons (holes) occupy states near the bottom (top) of the valleys, and states needed for absorption are once again available; the probe transmission then decreases. This is summarized in pictorial terms in Fig. 7.

## II. THEORY

### A. Electron and hole distributions

In the Introduction, we argued that the electron and hole populations in our problem can be described by two Fermi distributions which can be assigned the same temperature because of the rapid Coulomb collisions. Electrons and holes have distinct Fermi energies. Thus

$$f_{c\Gamma}(\vec{k}) = \left[1 + \exp\left(\frac{\mathcal{E}_{c\Gamma}(\vec{k}) - \epsilon}{\mathcal{T}}\right)\right]^{-1},$$

$$\mathcal{E}_0 \leq \mathcal{E}_{c\Gamma}(\vec{k}) < +\infty, \quad \text{(1a)}$$

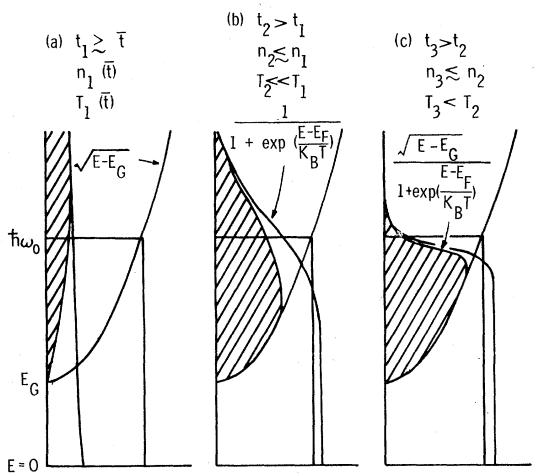


FIG. 7. Schematic diagram for the temporal evolution of the free carriers created by the excitation pulse.

$$f_{cL,X}(\vec{k}) = \left[1 + \exp\left(\frac{\mathcal{E}_{cL,X}(\vec{k}) - \epsilon}{\mathcal{T}}\right)\right]^{-1},$$

$$\mathcal{E}_G \leq \mathcal{E}_{cL,X}(\vec{k}) < +\infty, \quad (1b)$$

and likewise for the holes

$$f_H(\vec{k}) = \left[1 + \exp\left(\frac{\mathcal{E}_H(\vec{k}) + h}{\mathcal{T}}\right)\right]^{-1}, \quad 0 \leq \mathcal{E}_H(\vec{k}) < +\infty . \quad (1c)$$

Here, all energies are normalized with respect to $\hbar\omega_0$, where $\omega_0$ is the circular frequency of the optical pulse. The subscript $c\Gamma$ denotes the $\Gamma$ valley of the conduction band, $cL,X$ the $L$-$X$ valleys of the conduction band, and $H$ the holes in the valence bands. $\epsilon$ and $h$ are the normalized Fermi energies of the electrons and holes, respectively; and $\mathcal{E}_0$ and $\mathcal{E}_G$ are the normalized energies of the direct and indirect energy gaps, respectively. In the reduced Ge energy-band structure, the indirect energy gap is taken to be $\mathcal{E}_G \equiv \frac{1}{14}(8\mathcal{E}_L + 6\mathcal{E}_X)$, where $\mathcal{E}_L$ is the normalized energy band gap at $L$ and $\mathcal{E}_X$ is the normalized energy band gap at $X$. As discussed earlier we will treat the $L$ and the $X$ valleys as equivalent and assume that they have spheroid parabolic band structure. This simplifies the algebra considerably, but does not make much difference in the end results. Also note that, due to the rapid phonon-induced scattering of electrons between the central and the side conduction-band valleys (see Appendix A), we have taken the $\Gamma$ valley and the $L$- and $X$-valley Fermi energies to be identical. In the reduced band structure, electron and hole energies are given by

$$\mathcal{E}_{cL,X}(\vec{k}) = (1/\hbar\omega_0)[E_G + \hbar^2(\vec{k} - \vec{k}_{L,X})^2/2m_c]$$

$$\equiv \mathcal{E}_G + \hbar^2(\vec{k} - \vec{k}_{L,X})^2/2\hbar\omega_0 m_c , \quad (2a)$$

$$\mathcal{E}_{c\Gamma}(\vec{k}) = (1/\hbar\omega_0)(E_0 + \hbar^2k^2/2m_0)$$

$$\equiv \mathcal{E}_0 + \hbar^2k^2/2\hbar\omega_0 m_0 , \quad (2b)$$

$$\mathcal{E}_H(\vec{k}) = \hbar^2k^2/2\hbar\omega_0 m_h , \quad (2c)$$

and

$$h = E_H/\hbar\omega_0 , \quad \epsilon = E_F/\hbar\omega_0 , \quad \mathcal{T} = k_BT/\hbar\omega_0 . \quad (2d)$$

Here $\vec{k}$ is a wave vector, $k_B$ Boltzmann's constant, $m_0$ the effective mass for the $\Gamma$ valley, $m_c$ the effective mass for both the $L$ and the $X$ valleys, and $m_h$ the effective mass for the heavy-hole bands. $\vec{k}_{L,X}$ refer to the wave vectors for the minima of the conduction bands. The distributions defined above will depend on time through $\epsilon$, $h$, and $\mathcal{T}$. The Fermi energies $h$ and $\epsilon$ are related since the total number of electrons is equal to the total number of holes at all times.

In the present work, it is convenient to measure the electron density in terms of $N_0$, which is defined by

$$N_0 = \epsilon_\infty m\omega_0^2/4\pi e^2 , \quad (3)$$

where $\epsilon_\infty$ is the high-frequency dielectric constant, $e$ the electron charge, and $m$ the bare electron mass. Let us note that due to its smaller effective mass and higher band gap, the $\Gamma$ valley has a negligible density of electrons compared to the $L$-$X$ valleys. Thus, neglecting the $\Gamma$ valley and considering the effective mass of each of the four $L$ valleys to be equal to that of each of the six $X$ valleys, the total electron density is calculated as ten times the density in any one valley. The electron density is given by

$$n = \mathcal{T}^{3/2}\rho_1(z_1) , \quad (4a)$$

where the $\rho$'s and the $z$'s are defined in Table I. Likewise, the hole density is given by

$$n = \mathcal{T}^{3/2}\rho_2(z_2) \quad (4b)$$

and $\rho_2(z_2) = \rho_1(z_1)$ gives the integral relation between $\epsilon$ and $h$.

By taking the electron and hole distributions to be time dependent only, rather than dependent on

TABLE I. Definitions of integrals.

$$F(x) = (1 + e^x)^{-1}$$

$$\kappa(x) = \int_0^\infty dy\, yF(y + x)$$

$$\rho_i(x) = A_i \int_0^\infty dy\, y^{1/2}F(y + x)$$

$$\sigma_i(x) = A_i \int_0^\infty dy\, y^{1/2}[F(y + x)]^2$$

$$\nu_i(x) = A_i \int_0^\infty dy\, y^{3/2}F(y + x)$$

$$\zeta_j(x) = \int_0^\infty dy \{[(y+1)^{1/2} + (y)^{1/2}]^{4+j} - [(y+1)^{1/2} - (y)^{1/2}]^{4+j}\} \times \left[F\left(x + \left(\frac{y}{\mathcal{T}}\right)\right) - F\left(x + \left(\frac{y+1}{\mathcal{T}}\right)\right)\right]$$

$$A_1 = (5/\pi^2N_0)(2m_c\omega_0/\hbar)^{3/2}$$

$$A_2 = (1/\pi^2N_0)(2m_h\omega_0/\hbar)^{3/2}$$

$$A_3 = (1/2\pi^2N_0)(2m_0\omega_0/\hbar)^{3/2}$$

$$z_1 = (\mathcal{E}_G - \epsilon)/\mathcal{T}$$

$$z_2 = h/\mathcal{T}$$

$$z_3 = (\mathcal{E}_0 - \epsilon)/\mathcal{T}$$

$$z_4 = [\mathcal{E}_0 + (m_h/m_0 + m_h)(1 - \mathcal{E}_0) - \epsilon]/\mathcal{T}$$

$$z_5 = [(m_0/m_0 + m_h)(1 - \mathcal{E}_0) + h]/\mathcal{T}$$

$$z_6 = [\mathcal{E}_0 - (\mathcal{E}_G/2) + (\mathcal{T}_L/2)\ln(A_1/A_2)]/\mathcal{T}_L$$

both time and space, we are ignoring the pulse propagation problem within the interaction region (spot area times the sample thickness) as far as the electronic structure is concerned. This physically reasonable assumption will be justified and its consequences will be detailed in a subsequent paper dealing with the pulse propagation problem. The distributions defined in Eqs. (1a)–(1c) should be viewed as spatial averages of the actual distributions over the interaction region.

We also take the photon density within the interaction region to be time (but not space) dependent: $N_{\vec{q}}^{(\mathrm{rad})} = N_{\vec{q}}^{(\mathrm{rad})}(t)$. In addition, we assume that all quanta have the same wave vector. The radiation energy density at time $t$ is then given by

$$W(t) = \sum_{\vec{q}} \hbar\omega_q N_q^{(\mathrm{rad})}(t) \simeq \hbar\omega_0 N_0^{(\mathrm{rad})}(t) \equiv \hbar\omega_0 N_0 N(t) ,$$

where $N(t)$ is a normalized "photon" number density. Just as with the electron density, $N(t)$ should be viewed as a spatial average of the actual radiation density over the interaction region.

The following equations (for the electron-hole distributions) summarize the discussion of Sec. I:

$$\frac{d}{dt} f_{c\Gamma}(\vec{k}) = \left(\frac{\partial f_{c\Gamma}}{\partial t}\right)_{\mathrm{DA}} + \left(\frac{\partial f_{c\Gamma}}{\partial t}\right)_{\mathrm{FCA}} + \sum_j \left(\frac{\partial f_{c\Gamma}}{\partial t}\right)_{\Gamma\rightarrow j} + \left(\frac{\partial f_{c\Gamma}}{\partial t}\right)_{\mathrm{REL}} + \left(\frac{\partial f_{c\Gamma}}{\partial t}\right)_{R} , \tag{5a}$$

$$\frac{d}{dt} f_{cj}(\vec{k}) = -\left(\frac{\partial f_{c\Gamma}}{\partial t}\right)_{\Gamma\rightarrow j} + \left(\frac{\partial f_{cj}}{\partial t}\right)_{\mathrm{FCA}} + \left(\frac{\partial f_{cj}}{\partial t}\right)_{\mathrm{REL}} , \tag{5b}$$

$$\frac{d}{dt} f_H(\vec{k}) = \left(\frac{\partial f_H}{\partial t}\right)_{\mathrm{DA}} + \left(\frac{\partial f_H}{\partial t}\right)_{\mathrm{FCA}} + \left(\frac{\partial f_H}{\partial t}\right)_{\mathrm{REL}} + \left(\frac{\partial f_H}{\partial t}\right)_{R} , \tag{5c}$$

where DA represents the direct absorptions; FCA, the free-carrier absorptions; $\Gamma \rightarrow j$, the phonon-assisted scattering from the $\Gamma$ valley to the $j$ valley; REL, the intravalley relaxation of electrons and holes by means of emission or absorption of phonons; and $R$, the direct plasmon-assisted recombination. We note that the direct absorption terms mainly contribute to an increase in the carrier number. The free-carrier absorption contributions serve to increase the distribution temperature. The intravalley phonon-assisted relaxation terms decrease the distribution temperature. The direct recombination terms decrease the electron number and increase the distribution temperature. The $\Gamma \rightarrow j$ scattering terms do not change the electron number or significantly change the electron temperature; rather, they serve to populate the side valleys in the conduction band.

The behavior of the Fermi distributions for both electrons and holes is determined if $\epsilon$, $h$, and $\mathcal{T}$ are known at all times. Rather than dealing directly with the distribution functions, we will derive another set of equations from (5a)–(5c), which will describe the behavior of $\epsilon$, $h$, and $\mathcal{T}$ with time. For this purpose, we consider the time evolution of the electron density, which is given by

$$\frac{dn}{dt} = \tilde{\sum_{\vec{k}}} \frac{d}{dt} f_{c\Gamma}(\vec{k}) + \sum_j \tilde{\sum_{\vec{k}}} \frac{d}{dt} f_{cj}(\vec{k}) , \tag{6a}$$

where $j$ denotes a summation over all conduction-band side valleys. $\tilde{\sum}_{\vec{k}}$ includes the spin summation and the normalization factor, i.e.,[13]

$$\tilde{\sum_{\vec{k}}} = \int \frac{2d\vec{k}}{(2\pi)^3 N_0} .$$

We substitute Eqs. (5a) and (5b) into Eq. (6a), and recognizing that the free-carrier, $\Gamma \rightarrow j$ scattering, and the relaxation terms do not affect the electron density, we obtain the result

$$\frac{dn}{dt} = \tilde{\sum_{\vec{k}}} \left(\frac{\partial f_{c\Gamma}(\vec{k})}{\partial t}\right)_{\mathrm{DA}} + \tilde{\sum_{\vec{k}}} \left(\frac{\partial f_{c\Gamma}(\vec{k})}{\partial t}\right)_{R} . \tag{6b}$$

Inspection of Eq. (4a) shows that $n$ is a function of time via $\epsilon$ and $\mathcal{T}$. Thus we can also write

$$\frac{dn}{dt} = \left(\frac{\partial n}{\partial \epsilon}\right)_{\mathcal{T}} \frac{d\epsilon}{dt} + \left(\frac{\partial n}{\partial \mathcal{T}}\right)_{\epsilon} \frac{d\mathcal{T}}{dt} . \tag{6c}$$

We define

$$\gamma_\epsilon \equiv \left(\frac{\partial n}{\partial \epsilon}\right)_{\mathcal{T}} \quad \text{and} \quad \gamma_{\mathcal{T}} \equiv \left(\frac{\partial n}{\partial \mathcal{T}}\right)_{\epsilon} . \tag{7}$$

In terms of the integrals defined in Table I, we obtain

$$\gamma_\epsilon(t) = \mathcal{T}^{1/2}\rho_1(z_1) - \mathcal{T}^{1/2}\sigma_1(z_1) \tag{8}$$

and

$$\gamma_{\mathcal{T}}(t) = \tfrac{3}{2}\mathcal{T}^{1/2}\rho_1(z_1) + z_1\mathcal{T}^{1/2}[\rho_1(z_1) - \sigma_1(z_1)] . \tag{9}$$

Therefore, combining Eqs. (6b) and (6c) we write

$$\gamma_\epsilon(t)\frac{d\epsilon}{dt} + \gamma_{\mathcal{T}}(t)\frac{d\mathcal{T}}{dt} = \tilde{\sum_{\vec{k}}} \frac{\partial f_{c\Gamma}(\vec{k})}{\partial t}\bigg|_{\mathrm{DA}} + \tilde{\sum_{\vec{k}}} \frac{\partial f_{c\Gamma}(\vec{k})}{\partial t}\bigg|_{R} . \tag{10}$$

The fact that the number of electrons equals the number of holes requires that

$$\frac{dn}{dt} = \left(\frac{\partial n}{\partial h}\right)_{\mathcal{T}} \frac{dh}{dt} + \left(\frac{\partial n}{\partial \mathcal{T}}\right)_{h} \frac{d\mathcal{T}}{dt} = \left(\frac{\partial n}{\partial \epsilon}\right)_{\mathcal{T}} \frac{d\epsilon}{dt} + \left(\frac{\partial n}{\partial \mathcal{T}}\right)_{\epsilon} \frac{d\mathcal{T}}{dt} . \tag{11}$$

We define

$$\gamma_{\epsilon h} \equiv -\left(\frac{\partial n}{\partial \epsilon}\right)_{\mathcal{T}} \Big/ \left(\frac{\partial n}{\partial h}\right)_{\mathcal{T}} ;$$

$$\gamma_{\mathcal{T}h} \equiv \left[\left(\frac{\partial n}{\partial \mathcal{T}}\right)_{\epsilon} - \left(\frac{\partial n}{\partial \mathcal{T}}\right)_{h}\right] \Big/ \left(\frac{\partial n}{\partial h}\right)_{\mathcal{T}} . \tag{12}$$

Then, from (11) and (12) we have

$$\frac{dh}{dt} = -\gamma_{\epsilon h}(t)\frac{d\epsilon}{dt} + \gamma_{\mathcal{T}h}(t)\frac{d\mathcal{T}}{dt} . \tag{13}$$

Expressions for $\gamma_{\epsilon h}$ and $\gamma_{\mathcal{T}h}$ are evaluated by differentiating Eqs. (4a) and (4b). In terms of the integrals defined in Table I, these expressions are

$$\gamma_{\epsilon h}(t) = [\rho_1(z_1) - \sigma_1(z_1)] / [\rho_1(z_1) - \sigma_2(z_2)] \tag{14}$$

and

$$\gamma_{\mathcal{T}h}(t) = z_2 - z_1\gamma_{\epsilon h}(t) . \tag{15}$$

To this point, we have obtained two differential equations, (10) and (13), relating three unknowns: $\epsilon$, $h$, $\mathcal{T}$. We wish to find still a third independent differential equation relating these variables. We accomplish this by considering the energy density of the electrons and holes. The energy density of the electrons and holes, normalized by the photon energy $\hbar\omega_0$ and the number density $N_0$, is given by

$$u = \frac{U}{\hbar\omega_0 N_0} = \sum_j \tilde{\sum_{\vec{k}}} \left(\frac{E_{cj}(\vec{k})}{\hbar\omega_0}\right) f_{cj}(\vec{k}) + 2\tilde{\sum_{\vec{k}}} \left(\frac{E_H(\vec{k})}{\hbar\omega_0}\right) f_H(\vec{k}) + \tilde{\sum_{\vec{k}}} \left(\frac{E_{c\Gamma}(\vec{k})}{\hbar\omega_0}\right) f_{c\Gamma}(\vec{k}) \tag{16}$$

and $du/dt$ by

$$\frac{du}{dt} = \tilde{\sum_{\vec{k}}} \mathcal{E}_{c\Gamma}(\vec{k}) \frac{df_{c\Gamma}(\vec{k})}{dt} + \tilde{\sum_{\vec{k}}} \sum_j \mathcal{E}_{cj}(\vec{k}) \frac{df_{cj}(\vec{k})}{dt} + 2\tilde{\sum_{\vec{k}}} \mathcal{E}_H(\vec{k}) \frac{df_H(\vec{k})}{dt} . \tag{17}$$

The energy lost to the lattice due to $\Gamma \rightarrow j$ phonon-assisted scattering events is negligible. As discussed earlier, plasmon-assisted recombinations do not change $u$. Radiative recombinations would decrease the total energy, but they are negligible. The free-carrier absorption and phonon-assisted intravalley relaxation contributions of the $\Gamma$ valley to the energy are negligible compared to those of the $L$ and $X$ valleys. The following equations summarize these statements:

$$\frac{du}{dt} = \left(\frac{\partial u}{dt}\right)_{\mathrm{DA}} + \left(\frac{\partial u}{\partial t}\right)_{\mathrm{FCA}} + \left(\frac{\partial u}{\partial t}\right)_{\mathrm{REL}} , \tag{18a}$$

where

$$\left.\frac{\partial u}{\partial t}\right|_{\mathrm{DA}} = \tilde{\sum_{\vec{k}}} \mathcal{E}_{c\Gamma}(\vec{k}) \left(\frac{\partial f_{c\Gamma}(\vec{k})}{\partial t}\right)_{\mathrm{DA}} + 2\tilde{\sum_{\vec{k}}} \mathcal{E}_H(\vec{k}) \left(\frac{\partial f_H(\vec{k})}{\partial t}\right)_{\mathrm{DA}} , \tag{18b}$$

$$\left.\frac{\partial u}{\partial t}\right|_{\mathrm{FCA}} = \tilde{\sum_{\vec{k}}} \sum_j \mathcal{E}_{cj}(\vec{k}) \left(\frac{\partial f_{cj}(\vec{k})}{\partial t}\right)_{\mathrm{FCA}} + 2\tilde{\sum_{\vec{k}}} \mathcal{E}_h(\vec{k}) \left(\frac{\partial f_H(\vec{k})}{\partial t}\right)_{\mathrm{FCA}} , \tag{18c}$$

$$\left.\frac{\partial u}{\partial t}\right|_{\mathrm{REL}} = \tilde{\sum_{\vec{k}}} \sum_j \mathcal{E}_{cj}(\vec{k}) \left(\frac{\partial f_{cj}(\vec{k})}{\partial t}\right)_{\mathrm{REL}} + 2\tilde{\sum_{\vec{k}}} \mathcal{E}_H(\vec{k}) \left(\frac{\partial f_H(\vec{k})}{\partial t}\right)_{\mathrm{REL}} . \tag{18d}$$

Since $u = u(\epsilon, h, \mathcal{T})$ we can write

$$\frac{du}{dt} = \left(\frac{\partial u}{\partial \epsilon}\right)_{\mathcal{T},h}\frac{d\epsilon}{dt} + \left(\frac{\partial u}{\partial h}\right)_{\mathcal{T},\epsilon}\frac{dh}{dt} + \left(\frac{\partial u}{\partial \mathcal{T}}\right)_{\epsilon,h}\frac{d\mathcal{T}}{dt} . \tag{19a}$$

Making use of the definitions of $\gamma_{\epsilon h}$ and $\gamma_{\mathcal{T}h}$, we obtain

$$\frac{du}{dt} = \left[\left(\frac{\partial u}{\partial \epsilon}\right)_{\mathcal{T},h} - \left(\frac{\partial u}{\partial h}\right)_{\mathcal{T},\epsilon}\gamma_{\epsilon h}\right]\frac{d\epsilon}{dt} + \left[\left(\frac{\partial u}{\partial \mathcal{T}}\right)_{\epsilon,h} + \left(\frac{\partial u}{\partial h}\right)_{\mathcal{T},\epsilon}\gamma_{\mathcal{T}h}\right]\frac{d\mathcal{T}}{dt} . \tag{19b}$$

We define

$$\gamma_{u\epsilon} \equiv \left(\frac{\partial u}{\partial \epsilon}\right)_{\mathcal{T},h} - \gamma_{\epsilon h}\left(\frac{\partial u}{\partial h}\right)_{\mathcal{T},\epsilon} \tag{19c}$$

and

$$\gamma_{u\mathcal{T}} \equiv \left(\frac{\partial u}{\partial \mathcal{T}}\right)_{\epsilon,h} + \gamma_{\mathcal{T}h}\left(\frac{\partial u}{\partial h}\right)_{\mathcal{T},\epsilon} . \tag{19d}$$

Thus combining Eqs. (18a) and (19b), we find that

$$\gamma_{u\epsilon}(t)\frac{d\epsilon}{dt} + \gamma_{u\mathcal{T}}(t)\frac{d\mathcal{T}}{dt} = \left.\frac{\partial u}{\partial t}\right|_{\mathrm{DA}} + \left.\frac{\partial u}{\partial t}\right|_{\mathrm{FCA}} + \left.\frac{\partial u}{\partial t}\right|_{\mathrm{REL}} . \tag{20}$$

Let us note that in the evaluation of $\gamma_{u\epsilon}$ and $\gamma_{u\mathcal{T}}$, the $\Gamma$ valley can be neglected just as in the case of electron density, and for the same reasons. Thus in terms of the integrals of Table I,

$$\gamma_{u\epsilon}(t) = \tfrac{3}{2}\mathcal{T}^{3/2}\rho_1(z_1)(1+\gamma_{\epsilon h}) + \mathcal{T}^{1/2}\mathcal{E}_G[\rho_1(z_1) - \sigma_1(z_1)] \tag{21}$$

and

$$\gamma_{u\mathcal{T}}(t) = \mathcal{T}^{1/2}\mathcal{E}_G[(\tfrac{3}{2}+z_1)\rho_1(z_1) - z_1\sigma_1(z_1)] + \tfrac{5}{2}\mathcal{T}^{3/2}[\nu_1(z_1) + \nu_2(z_2) + \tfrac{3}{5}z_1\rho_1(z_1)(1+\gamma_{\epsilon h})] . \tag{22}$$

Let us also note that when the $\Gamma$ valley is neglected,

$$u(t)=\mathcal{T}^{5/2}[\nu_1(z_1)+\nu_2(z_2)]+\mathcal{T}^{3/2}\mathcal{G}_G\rho_1(z_1). \tag{23}$$

Summarizing, Eqs. (10), (13), and (20) are a coupled set of differential equations describing the time evolution of the Fermi energies, $\epsilon$ and $h$ and carrier temperature $\mathcal{T}$. For convenience, we summarize our working equations below:

$$\gamma_\epsilon(t)\frac{d\epsilon}{dt}+\gamma_{\mathcal{T}}(t)\frac{d\mathcal{T}}{dt}=\sum_{\vec{k}}\frac{\partial f_{c\Gamma}(\vec{k})}{\partial t}\bigg|_{DA}+\sum_{\vec{k}}\frac{\partial f_{c\Gamma}(\vec{k})}{\partial t}\bigg|_{R}, \tag{10}$$

$$\frac{dh}{dt}=-\gamma_{eh}(t)\frac{d\epsilon}{dt}+\gamma_{\mathcal{T}h}(t)\frac{d\mathcal{T}}{dt}, \tag{13}$$

$$\gamma_{u\epsilon}(t)\frac{d\epsilon}{dt}+\gamma_{u\mathcal{T}}(t)\frac{d\mathcal{T}}{dt}=\frac{\partial u}{\partial t}\bigg|_{DA}+\frac{\partial u}{\partial t}\bigg|_{FCA}+\frac{\partial u}{\partial t}\bigg|_{REL}. \tag{20}$$

As the light is absorbed the carrier density and temperature pass through a region in which neither the low-temperature approximation nor the high-temperature approximation holds; as a result we must evaluate these expressions numerically. First, we must turn our attention to calculating the absorption and relaxation rates appearing on the right-hand sides of Eqs. (10) and (20).

### B. Direct absorption

In this and Secs. II C and II D we will confine ourselves to presenting only the results in order not to burden the discussion with too much algebra. Direct and free-carrier absorptions in Ge are dealt with extensively in the literature.[14-20] As mentioned earlier, a number of simplifying approximations can be made in our problem. For this reason we discuss the appropriate electron-photon and electron-phonon coupling Hamiltonians in the text, and present a detailed summary of the calculation in Appendix C. The appropriate diagrams describing the perturbation terms used in the calculation are shown in Figs. 8 and 9. We confine ourselves to the lowest-order perturbation terms described by these diagrams, higher-order terms being negligible.

The diagrams in Fig. 8 describe direct absorption and emission (of a quantum $\hbar\omega_0$). The electron-phonon coupling is described by the well-known Hamiltonian

$$H_1=\sum_{\lambda\vec{q};s\vec{k};s'\vec{k}'}\left(\frac{e}{mc}\right)\left(\frac{2\pi c^2\hbar}{\epsilon_\infty\omega_q}\right)^{1/2}\langle s'\vec{k}'|\times e^{i\vec{q}\cdot\vec{r}}\hat{\xi}_\lambda(\vec{q})\cdot\vec{p}\,|s\vec{k}\rangle c^\dagger_{s'\vec{k}'}c_{s\vec{k}}b_{\lambda q}+\text{H.c.}, \tag{24}$$

where $|s\vec{k}\rangle$ refers to Bloch states ($s$ is the band index); $\hat{\xi}_\lambda(\vec{q})$ is the unit photon polarization vector;

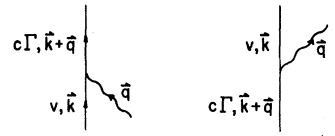


FIG. 8. Direct optical transitions. Solid lines refer to electrons or holes, wavy lines to photons.

$\vec{p}$ is the electron momentum operator; $c_{s\vec{k}}$ and $b_{\lambda q}$ are the electron and photon annihilation operators, respectively. Electron momenta are generally much larger than the photon momentum; thus

$$\langle s'\vec{k}'|e^{i\vec{q}\cdot\vec{r}}\hat{\xi}_\lambda(\vec{q})\cdot\vec{p}\,|s\vec{k}\rangle\simeq\hat{\xi}_\lambda(\vec{q})\cdot\langle s'\vec{k}'|\vec{p}\,|s\vec{k}\rangle. \tag{25a}$$

For direct absorption, generally the absolute square of the interband matrix element of the momentum operator $|\langle c\vec{k}|\vec{p}\,|v\vec{k}\rangle|^2$ is needed. This quantity can be evaluated with the help of the so-called $f$-sum rule.[21] Near the $\Gamma$-valley band edge (BE)

$$|\langle c\vec{k}|\vec{p}\,|v\vec{k}\rangle|^2\simeq\tfrac{1}{2}m^2E_0(1/m_0+1/m_h)\equiv m^2E_0/2m_{BE}. \tag{25b}$$

The laser frequency $\hbar\omega_0$ is such that the direct absorptions will involve the $\Gamma$ valley and the heavy-hole bands only. The direct absorptions due to the transitions between the light-hole band and the heavy-hole bands are neglibible since such transitions are restricted to regions away from the center of the Brillouin zone and thus restricted by the Fermi statistical factors, and since the density of the states of the light-hole band is small.

Using (24) and (25) with the help of the diagrams shown in Fig. 8 and the approximations indicated in Appendix C, one finds

$$\sum_{\vec{k}}\frac{\partial f_{c\Gamma}(\vec{k})}{\partial t}\bigg|_{DA}=N(t)\alpha_D(t), \tag{26}$$

$$\frac{\partial u}{\partial t}\bigg|_{DA}=N(t)\alpha_D(t), \tag{27}$$

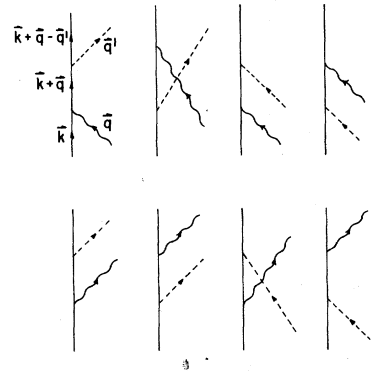


FIG. 9. Free-carrier transitions. Broken lines refer to phonons.

and

$$\left.\frac{\partial N}{\partial t}\right|_{DA} = -N(t)\alpha_D(t), \tag{28}$$

where

$$\alpha_D(t) = \alpha_0[1 - F(z_4) - F(z_5)], \tag{29}$$

and

$$\alpha_0 = \frac{4e^2\mathcal{E}_0}{3\epsilon_\infty\hbar^2}\left(\frac{2m_0m_h\hbar\omega_0(1-\mathcal{E}_0)}{(m_0+m_h)}\right)^{1/2}. \tag{30}$$

$z_4$, $z_5$, and $F$ are defined in Table I. $N(t)$ is the normalized photon density in the interaction region mentioned earlier. $\alpha_D(t)$ is the direct absorption rate. $(\sqrt{\epsilon_\infty}/c)\alpha_0$ is the usual absorption coefficient (per unit length) observed in Beer's-law region[7] (for the light frequency $\omega_0$).

In Fig. 10, $\alpha_D/\alpha_0$ is plotted as a function of electron-hole temperature for fixed electron-hole densities. The effective masses and the energy-gap parameters are the same for all the curves in the figure.

We observe that as the density decreases, $\alpha_D/\alpha_0$ approaches 1 for all $\mathcal{T}$:

$$\lim_{n\to 0}\alpha_D = \alpha_0. \tag{31}$$

Also $\alpha_D$ has the same behavior for all densities as $\mathcal{T}\to\infty$, which is to be expected since as $\mathcal{T}$ increases the probability for the occupancy of a given conduction state decreases to essentially zero, thus

$$\lim_{\mathcal{T}\to\infty}\alpha_D = \alpha_0. \tag{32}$$

As $\mathcal{T}\to 0$, $\alpha_D$ shows interesting structure. We see that there are two critical densities such that

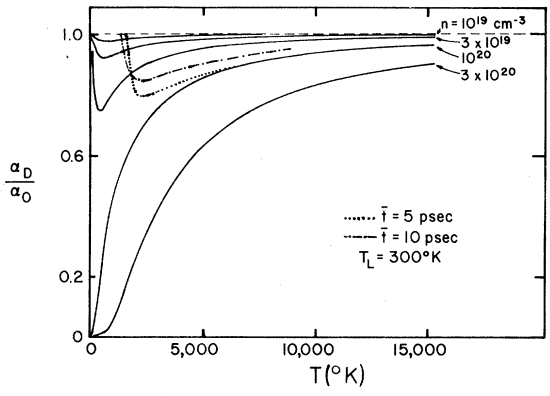


FIG. 10. Direct absorption coefficient vs electron-hole temperature. The curves are generated for the gap parameters corresponding to $T_L = 300\,^\circ$K. The dotted and dashed curves refer to possible trajectories in this $n$, $\mathcal{T}$ space as the pulse passes through the sample.

$$\lim_{\mathcal{T}\to 0}\alpha_D = \begin{cases} \alpha_0 & \text{if } n<n_1, \\ \frac{1}{2}\alpha_0 & \text{if } n=n_1, \\ 0 & \text{if } n_1<n<n_2, \\ -\frac{1}{2}\alpha_0 & \text{if } n=n_2, \\ -\alpha_0 & \text{if } n_2<n, \end{cases} \tag{33}$$

where $n_1$ and $n_2$ are given by

$$n_1N_0 = \frac{2}{3\pi^2\hbar^3}\left(\frac{2m_0m_h}{m_0+m_h}(\hbar\omega_0 - E_0)\right)^{3/2} \tag{34a}$$

and

$$n_2N_0 = \frac{10}{3\pi^2\hbar^3}\left(\frac{2m_cm_h}{m_0+m_h}(\hbar\omega_0 - E_0) + 2m_c(E_0 - E_G)\right)^{3/2}. \tag{34b}$$

The existence of $n_1$ and $n_2$ can easily be inferred from Fig. 5. As $\mathcal{T}\to 0$, electrons collect at the bottom of the conduction-band valleys and holes at the top of the valence bands. When $n<n_1$ and $\mathcal{T}\to 0$, $E_F<E''$ and $E_H>E'$; thus direct absorptions can take place unimpeded and $\alpha_D\to\alpha_0$. When $n>n_1$ and $\mathcal{T}\to 0$, $E_H<E'$ and the valence-band states which can absorb $\hbar\omega_0$ quanta are empty. When $n>n_2$ and $\mathcal{T}\to 0$, $E_F>E''$ and $E_H<E'$, and thus the inverse of absorption, i.e., stimulated emission of $\hbar\omega_0$ quanta occurs, and $\alpha_D$ becomes $-\alpha_0$. The two densities $n_1$ and $n_2$ are large. For typical values of the effective masses and energy gaps, such as $m_0\simeq 0.1$, $m_h\simeq 0.34$, $m_c\simeq 0.22$, $E_G\sim 0.7$ eV and $E_0\sim 0.9$ eV, and $\hbar\omega_0 = 1.17$ eV, we find $n_1N_0\sim 4\times 10^{19}$ cm$^{-3}$ and $n_2N_0\sim 2\times 10^{21}$ cm$^{-3}$. In the experiment, the maximum electron densities achieved remain below $n_2$. Finally, we observe that for $n<n_1$, the minimum of $\alpha_D$ occurs at finite temperatures.

As we shall see later, the direct absorptions remain dominant compared to the free-carrier absorptions for all light intensities used in the experiment, and therefore, the qualitative features of the experimental results can easily be inferred from a diagram such as the one in[22] Fig. 10. $\epsilon_\infty \simeq 16$ for Ge.[23] Thus, for the effective-mass and energy-gap values quoted above, $\alpha_0\sim 9\times 10^{13}$ sec$^{-1}$. The usual (Beer's law) linear absorption coefficient is obtained from $\alpha_0$ by dividing by the speed of light in the absorbing medium, i.e.,

$$\alpha_{\text{Beer}} = (\sqrt{\epsilon_\infty}/c)\alpha_0 = 1.2\times 10^4\text{cm}^{-1},$$

in agreement with the well-known value.

### C. Free-carrier absorption

The electron-phonon interaction is described by the Hamiltonian

$$H_2 = \sum_{\mu,\vec{q}'} \sum_{s,\vec{k},\vec{k}'} \left(\frac{\hbar}{2\rho\Omega_{\mu\vec{q}'}}\right)^{1/2} \times Q_\mu \langle s\vec{k}' | e^{i\vec{q}'\cdot\vec{r}} | s\vec{k}\rangle c^\dagger_{s\vec{k}'} c_{s\vec{k}} a_{\mu\vec{q}'} + \text{H.c.}, \tag{35}$$

where $\mu$ varies over the phonon modes, $\rho$ is the Ge mass density, $\Omega_{\mu\vec{q}'}$ is the phonon frequency, $Q_\mu$ is the electron-phonon coupling coefficient, and $a_{\mu\vec{q}'}$ is the phonon annihilation operator. We note that for the Bloch states

$$\langle s\vec{k}' | e^{i\vec{q}'\cdot\vec{r}} | s\vec{k}\rangle \simeq \delta^3(\vec{k}' - \vec{k} - \vec{q}'), \tag{36a}$$

$$\langle s\vec{k}' | \vec{p} | s\vec{k}\rangle \simeq \hbar\vec{k}\delta^3(\vec{k}' - \vec{k}) , \tag{36b}$$

where $s$ refers to the conduction or the valence bands. Figure 9 illustrates typical free-carrier absorption diagrams. There are altogether 16 such diagrams. With the help of such diagrams and (35)–(36b), the rates $(\partial N/\partial t)$ and $(\partial u/\partial t)$ due to free-carrier absorption can be calculated as summarized in Appendix C. In those calculations, two plausable assumptions are made: (a) the same electron-phonon coupling coefficients are taken for the $L$ and the $X$ valleys; (b) the same coupling coefficients are used for the electrons and the holes. This procedure is followed for the purpose of simplifying the calculations, and can be justified only *a posteriori*, after comparison with the experimental results. Let $\phi_j$ be the angle between $\vec{q}'$ and the $j$th valley direction. The electron-phonon coupling coefficients are then as follows. For the longitudinal optical phonons[24]

$$Q_{\text{LO}} = Q_0 \cos\phi_j ; \tag{37a}$$

for transverse optical phonons

$$Q_{\text{TO}} = Q_0 \sin\phi_j ; \tag{37b}$$

for longitudinal acoustical phonons

$$Q_{\text{LA}}(\vec{q}') = q'(\Lambda_d + \Lambda_u \cos^2\phi_j) ; \tag{37c}$$

for transverse acoustical phonons

$$Q_{\text{TA}}(q') = -q'\Lambda_u \cos\phi_j \sin\phi_j . \tag{37d}$$

$Q_0$ is the electron–optical-phonon coupling constant. This coupling constant is taken to be dependent on lattice temperature: $Q_0 = 6\times10^{-4}$ at 300 °K and $Q_0 = 2\times10^{-4}$ at 77 °K. $\Lambda_d$ and $\Lambda_u$ are the same deformation potential constants as in Herring and Vogt.[25] Also, we assume a single reststrahl frequency for the optical phonons, and make a linear approximation for the acoustical phonons[26]:

$$\Omega_{\text{LO,TO}} \simeq \Omega_0, \tag{38a}$$

$$\Omega_{\text{LA,TA}} \simeq c_A q' . \tag{38b}$$

Free-carrier absorption depends upon the electron population. The Γ-valley electron population is negligible compared to that of the $L$ and $X$ valleys; therefore, the Γ valley is ignored in the FCA calculation. We also assume in Appendix C that each electron after a phonon-assisted photon absorption remains in the same valley, since the intervalley scattering rates among the $L$ and $X$ valleys are small.[27]

With these approximations and others indicated in Appendix C, we obtain the following expressions for the absorption rates:

$$\left.\frac{\partial N}{\partial t}\right|_{\text{FCA}} = -N(t)\alpha_{\text{FCA}}(t) , \tag{39}$$

$$\left.\frac{\partial u}{\partial t}\right|_{\text{FCA}} = N(t)\alpha_{\text{FCA}}(t) , \tag{40}$$

where

$$\alpha_{\text{FCA}}(t) = \{\alpha_1[1 + 2(\omega_0/\Omega_0)\mathcal{T}_L] + \alpha_2\mathcal{T}_L\} \times [\zeta_0(z_2) + 5(m_c/m_h)^2\zeta_0(z_1)] + \alpha_3[\zeta_1(z_2) + 5(m_c/m_h)^{5/2}\zeta_1(z_1)] , \tag{41a}$$

$$\alpha_1 = e^2Q_0^2m_h^2/3\pi^2\epsilon_\infty\rho\hbar^4\Omega_0 , \tag{41b}$$

$$\alpha_2 = 2e^2m_h^2\Lambda^2\omega_0/3\pi^2\epsilon_\infty\rho c_A^2\hbar^4 , \tag{41c}$$

$$\alpha_3 = 4e^2m_h^2\Lambda^2(2m_h\hbar\omega_0)^{1/2}/15\pi^2\epsilon_\infty\rho c_A\hbar^5 , \tag{41d}$$

$$\Lambda^2 = \Lambda_d^2 + \tfrac{2}{3}\Lambda_d\Lambda_u + \tfrac{1}{3}\Lambda_u^2 . \tag{41e}$$

For the definition of ζ functions see Table I. Here, $\mathcal{T}_L = k_BT_L/\hbar\omega_0$ is the normalized lattice temperature. For Ge, $\epsilon_\infty \simeq 16$, $\rho \simeq 5.3$ g/cm$^3$, $\Lambda_d \simeq -3.4$ eV, $\Lambda_u \simeq 17$ eV, $Q_0 \simeq 6\times10^{-4}$ erg/cm, $\hbar\Omega_0 \simeq 1.88\times10^{-2}$ eV, and $c_A \simeq 5.4\times10^5$ cm/sec at 300 °K. Using these values we find $\alpha_1 \approx 10^{11}$ sec$^{-1}$, $\alpha_2 \approx 2\times10^{13}$ sec$^{-1}$, and $\alpha_3 \approx 10^{11}$ sec$^{-1}$. Although $\alpha_2$ seems to be quite large compared to $\alpha_1$ and $\alpha_3$, actually $\alpha_2$ occurs in $\alpha_{\text{FCA}}$ as $\alpha_2\mathcal{T}_L$, and since generally $\mathcal{T}_L \sim 10^{-2}$, $\alpha_2\mathcal{T}_L$ is of the same order as $\alpha_3$. Note that

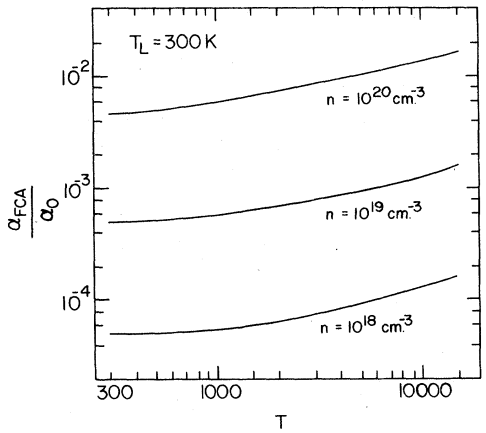


FIG. 11. Free-carrier absorption coefficient vs electron-hole temperature.

$\alpha_1$, $\alpha_2$, $\alpha_3$ are quite small compared to $\alpha_0 \sim 9\times10^{13}$ sec$^{-1}$.

Plots of $\alpha_{\mathrm{FCA}}$ as a function of $(\hbar\omega_0/k_B)\mathcal{T}(=T)$ for fixed $nN_0$ are given in Fig. 11. The behavior of $\alpha_{\mathrm{FCA}}$ can easily be deduced from (41) for low- and high-temperature limits. In the low-temperature limit (for fixed $n$)

$$\zeta_0(z_2)+5\left(\frac{m_c}{m_h}\right)^2\zeta_0(z_1) \simeq 8nN_0\left\{\frac{1}{A_2}\left[1+\left(\frac{3n}{2A_2}\right)^{2/3}\right]^{3/2} + \frac{5m_c^2}{m_h^2A_1}\left[1+\left(\frac{3n}{2A_1}\right)^{2/3}\right]^{3/2}\right\}. \quad (42)$$

For the values of the density that occur in the experiment $3n/2A_1<1$ and $3n/2A_2<1$, and therefore

$$\zeta_0(z_2)+5\left(\frac{m_c}{m_h}\right)^2\zeta_0(z_1)\simeq 8n\left(\frac{1}{A_2}+\frac{5m_c^2}{m_h^2A_1}\right)\approx 96n \quad (43)$$

and $\alpha_{\mathrm{FCA}}\propto n$. At large temperatures, i.e., as $\mathcal{T}\to\infty$,

$$\zeta_0(z_2)+5\left(\frac{m_c}{m_h}\right)^2\zeta_0(z_1)\to\frac{64}{\sqrt{\pi}}\left(\frac{1}{A_2}+\frac{5m_c^2}{A_1m_h^2}\right)n\mathcal{T}^{1/2} \approx 500n\mathcal{T}^{1/2} \quad (44a)$$

and

$$\zeta_1(z_2)+5\left(\frac{m_c}{m_h}\right)^{5/2}\zeta_1(z_1)\to 120\left[\frac{1}{A_2}+5\left(\frac{m_c}{m_h}\right)^{5/2}\right]n\mathcal{T} \approx 1000n\mathcal{T}. \quad (44b)$$

Therefore, as temperature increases, for a given $n$, $\alpha_{\mathrm{FCA}}$ begins to vary linearly with $\mathcal{T}$. We also observe that in both temperature limits $\alpha_{\mathrm{FCA}}\propto n$.

### D. Phonon-assisted relaxation

We are particularly interested in electron-hole *energy* relaxation via phonon emission and absorption, as it relates to the electron-hole temperature relaxation. The diagrams in Fig. 12 show phonon emission and absorption. As discussed earlier, electron and hole transitions are assumed to be intraband and intravalley in phonon-assisted relaxation. The calculation of $(\partial u/\partial t)_{\mathrm{REL}}$ from the diagrams of Fig. 12 is quite similar to the FCA calculation. As shown in Appendix D, we find

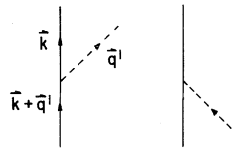


FIG. 12. Phonon-assisted relaxation.

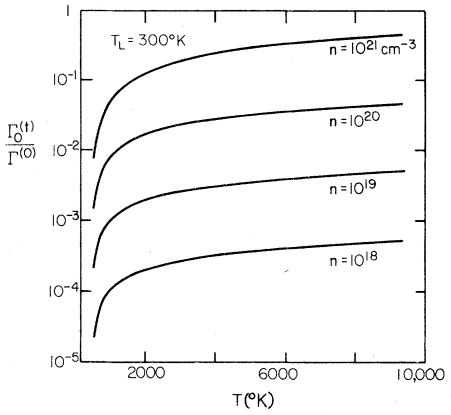


FIG. 13. Optical-phonon-assisted relaxation vs electron-hole temperature.

$$\left(\frac{\partial u}{\partial t}\right)_{\mathrm{REL}}=-[\Gamma_0(t)+\Gamma_A(t)]\,, \quad (45)$$

where

$$\Gamma_0(t)=\Gamma^{(0)}\mathcal{T}(\mathcal{T}-\mathcal{T}_L) \times[\ln(1+e^{-z_2})+5(m_c/m_h)^3\ln(1+e^{-z_1})]\,, \quad (46a)$$

$$\Gamma_A(t)=\Gamma^{(a)}\mathcal{T}^2(\mathcal{T}-\mathcal{T}_L)[\kappa(z_2)+5(m_c/m_h)^4\kappa(z_1)]\,, \quad (46b)$$

$$\Gamma^{(0)}=2Q_0^2m_h^3\omega_0/\rho\pi^3N_0\hbar^4\,, \quad (46c)$$

$$\Gamma^{(a)}=16\Lambda^2m_h^4\omega_0^2/\rho\pi^3N_0\hbar^5\,, \quad (46d)$$

and $\kappa(x)$ is defined in Table I. $\Gamma_0(t)$ is the relaxation rate due to the optical phonons, $\Gamma_A(t)$, due to the acoustical phonons. For Ge, $\Gamma^{(0)}\approx 2\times10^{10}$ sec$^{-1}$ and $\Gamma^{(a)}\approx 5\times10^{10}$ sec$^{-1}$ at 300 °K. Owing to the (linear) dispersion of acoustical phonons, the temperature dependence of $\Gamma_0(t)$ and $\Gamma_A(t)$ is different. Plots of $\Gamma_0(t)$ and $\Gamma_A(t)$ vs $(\hbar\omega_0/k_B)\mathcal{T}$ $(=T)$ are given in Figs. 13 and 14. For large temperatures (fixed $n$)

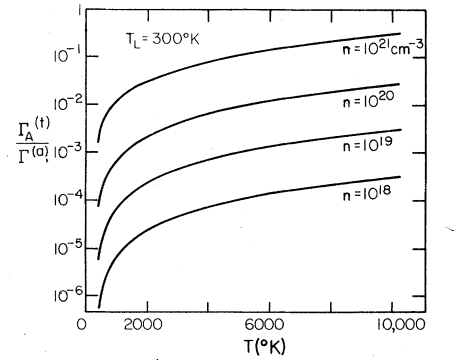


FIG. 14. Acoustical-phonon-assisted relaxation vs electron-hole temperature.

$$\lim_{\mathcal{T}\to\infty}\Gamma_0(t)\to\frac{2\Gamma^{(0)}[1+(m_c/m_h)^{3/2}]\mathcal{T}^{1/2}n}{A_2\sqrt{\pi}}$$

$$\approx 9\Gamma^{(0)}n\mathcal{T}^{1/2}\ , \tag{47a}$$

$$\lim_{\mathcal{T}\to\infty}\Gamma_A(t)\to\frac{2\Gamma^{(a)}[1+(m_c/m_h)^{5/2}]\mathcal{T}^{3/2}n}{A_2\sqrt{\pi}}$$

$$\approx 8\Gamma^{(a)}n\mathcal{T}^{3/2}\ ; \tag{47b}$$

thus, relaxation via acoustic-phonon emission and absorption becomes more important at high temperatures. In this limit, $\Gamma_0+\Gamma_A\propto n$. Since $\lim u\propto n$ as $\mathcal{T}\to\infty$, the rate of relaxation of $\mathcal{T}$ is independent of the density $n$ as $\mathcal{T}\to\infty$. On the other hand, when $\mathcal{T}$ is near $\mathcal{T}_L$ (but $n$ is much greater than the thermal equilibrium density),

$$\Gamma_0(t)\sim(3/2A_2)^{2/3}[1+\tfrac{1}{5}(A_1/A_2)^{4/3}]$$
$$\times\Gamma^{(0)}n^{2/3}(\mathcal{T}-\mathcal{T}_L)\approx 7\Gamma^{(0)}n^{2/3}(\mathcal{T}-\mathcal{T}_L)\ , \tag{48a}$$

$$\Gamma_A(t)\sim\tfrac{1}{2}(3/2A_2)^{4/3}[1+(1/5^{5/3})(A_1/A_2)^{4/3}]$$
$$\times\Gamma^{(a)}n^{4/3}(\mathcal{T}-\mathcal{T}_L)\approx 8\Gamma^{(a)}n^{4/3}(\mathcal{T}-\mathcal{T}_L)\ . \tag{48b}$$

Thus the density dependence of $\Gamma_0(t)$ and $\Gamma_A(t)$ is different. Note also that the relaxation of $\mathcal{T}$ is density dependent since $(\partial u/\partial\mathcal{T})_n\propto n^{1/3}$ in this limit.

The specific heat of the lattice is approximately constant for Ge.[23] Therefore

$$\frac{du_L}{dt}=-\left(\frac{\partial u}{\partial t}\right)_{\text{REL}}=c_L\frac{d\mathcal{T}_L}{dt}\ , \tag{49}$$

where $c_L=C_L/N_0k_B$ and $C_L$ is the specific heat of the Ge lattice in erg/cm$^3$ °K.[28] Thus

$$\frac{d\mathcal{T}_L}{dt}=\frac{1}{c_L}\left[\Gamma_0(t)+\Gamma_A(t)\right]\ . \tag{50}$$

The energy-gap parameters $\mathcal{E}_G$ and $\mathcal{E}_0$ are functions of $\mathcal{T}_L$. Therefore relaxation, in addition to retarding the growth of $\mathcal{T}$, will also influence $n$, $\epsilon$, etc., through the variation of $\mathcal{E}_G$ and $\mathcal{E}_0$ as $\mathcal{T}_L$ increases.

### E. Plasmon-assisted recombination

The combined electron-hole plasma frequency is given by

$$\omega_p^2=\frac{4\pi e^2n}{\epsilon_\infty}N_0\left(\frac{1}{m_c}+\frac{1}{m_h}\right)=\omega_0^2n\left(\frac{m}{m_c}+\frac{m}{m_h}\right)\ . \tag{51}$$

As the electron and hole densities build up $\omega_p$ increases in magnitude, becoming comparable to the Ge gap frequencies. The plasmon resonance is substantially broadened when the excitation pulse is passing through the sample. This is due to the fact that direct absorption populates only the $\Gamma$ valley. Therefore, the Fermi energy of the $\Gamma$-valley electrons is perturbed relative to the Fermi energy of the $L$-$X$ valley electrons when the excitation pulse is on. This relative perturbation is rapidly damped, as the two Fermi energies try to rapidly equalize by means of the phonon-assisted intervalley scatterings between the $\Gamma$ valley and the side valleys. It is just such rapid damping that causes the substantial broadening of the plasmon resonance. Note that Coulomb collisions (considered in Appendix B) are ineffective in transferring electrons between the $\Gamma$ valley and the side valleys, and thus would not damp the relative perturbation of the Fermi energies referred to above. Electrons and holes can of course relax via intravalley and intraband phonon emissions, and thus perturb the Fermi energies. But these are slow processes compared to the $\Gamma$-$L$,$X$ scattering. Their contribution to the plasmon resonance broadening is negligible.

As a result of the broadening of the plasmon resonance, plasmons have short lifetimes and plasmon emission will essentially be spontaneous rather than stimulated. An electron in the $\Gamma$ valley will recombine with a hole near the top of the valence bands via spontaneous emission of a plasmon. Largely long-wavelength plasmons will be emitted.[29]

For plasmons which have long wavelengths and *infinite* lifetime, the electron-plasmon coupling (in "random-phase approximation") is given by the Hamiltonian[30]

$$H_3\simeq -i\sum_{s\vec{k},s'\vec{k}',\vec{q}}\left(\frac{2\pi e^2\omega p}{q^2\epsilon_\infty}\right)^{1/2}$$
$$\times\langle s\vec{k}|e^{i\vec{q}\cdot\vec{r}}|s'\vec{k}'\rangle A_{\vec{q}}c^\dagger_{s\vec{k}}c_{s'\vec{k}'}+\text{H.c.}\ , \tag{52a}$$

where $A_{\vec{q}}$ is the annihilation operator for a plasmon of momentum $\vec{q}$. We are particularly interested in the interband transition terms (i.e., recombination terms) in (52a). Near the $\Gamma$-valley band edge, and again for long-wavelength plasmons ($\vec{q}\to 0$),

$$\langle c\vec{k}|e^{i\vec{q}\cdot\vec{r}}|v\vec{k}\rangle\simeq-[(\vec{q}\cdot\vec{P}_{cv})/mE_0]\delta^3(\vec{k}'-\vec{k}+\vec{q}), \tag{52b}$$

where $\vec{P}_{cv}=\langle c\vec{k}|\vec{p}|v\vec{k}\rangle$, the intraband matrix element of the momentum operator as in (25b). From $H_3$, we find that the recombination rate for a $\Gamma$-valley electron with momentum $\vec{k}$ via spontaneous emission of a plasmon (of infinite lifetime) is given by

$$\Gamma_R(\vec{k})=\sum_{v=1}^{2}\sum_{\vec{q}}\left(\frac{4\pi^2e^2\omega_p}{q^2\epsilon_\infty}\right)\left|\frac{\vec{q}\cdot\vec{P}_{cv}}{mE_0}\right|^2$$
$$\times\delta(E_c(\vec{k})-E_v(\vec{k}-\vec{q})-\hbar\omega_p). \tag{53}$$

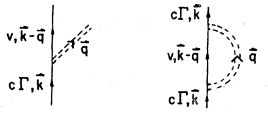


FIG. 15. Plasmon-assisted recombination. Double broken lines refer to plasmons.

However, in our problem, plasmons have a short lifetime, and therefore, the $\delta$ function in (53) is replaced by a Lorentzian. More precisely, (53) is replaced by[31]

$$\Gamma_R(\vec{k}) = \left(\frac{2}{\hbar}\right)\sum_{v=1}^{2}\int \frac{d^3\vec{q}}{(2\pi)^3}\left(\frac{4\pi e^2}{q^2\epsilon_\infty}\right)\left|\frac{\vec{q}\cdot\vec{P}_{cv}}{mE_0}\right|^2 \operatorname{Im}\left(\frac{-1}{\epsilon(\vec{q},[E_{c0}(\vec{k})-E_v(\vec{k}-\vec{q})]/\hbar)}\right), \tag{54}$$

where $\epsilon(\vec{q},\omega)=\epsilon_1(\vec{q},\omega)+i\epsilon_2(\vec{q},\omega)$ is the dielectric function. Equation (54) is obtained from the self-energy diagram shown in Fig. 15. We will approximate $\Gamma_R$ by the rate for those electrons and holes which are near the band edge at $\Gamma$; i.e., we set $k=0$ and $E_{c0}-E_v=E_0+\hbar^2q^2/2m_h$. We will also assume a high-frequency Drude form for the dielectric function:

$$\epsilon(\omega)=1-\frac{\omega_p^2}{\omega(\omega+i/\tau_0)}. \tag{55}$$

$\delta_{pl}\equiv\hbar/2\tau_0$ represents the plasmon resonance broadening mentioned earlier [see Eqs. (56c) and (56d)]. We set $(2/\hbar)\delta_{pl}$ equal to the $\Gamma\to L,X$ scattering rate calculated in Appendix A:

$$\frac{1}{\tau_0}=\frac{5(2m_c)^{3/2}(Q_0^2+Q_A^2)(\hbar\omega_0-E_G)^{1/2}}{2\pi\rho\Omega_0\hbar^3}. \tag{A3}$$

When the plasmon-assisted recombinations are appreciable, electron and hole densities are sufficiently large that $\omega_p\tau_0>1$, and near the plasmon pole ($\omega\sim\omega_p$)

$$\epsilon_1(\omega)\simeq 1-\omega_p^2/\omega^2\simeq(2/\omega_p)(\omega-\omega_p), \tag{56a}$$

$$\epsilon_2(\omega)\simeq 1/\omega_p\tau_0, \tag{56b}$$

$$\operatorname{Im}\left(\frac{-1}{\epsilon(E_0/\hbar+\hbar q^2/2m_h)}\right) \simeq\frac{\hbar\omega_p}{2}\left(\frac{\hbar/2\tau_0}{(\hbar\omega_p-E_0-\hbar^2q^2/2m_h)^2+(\hbar/2\tau_0)^2}\right). \tag{56c}$$

From these approximations and (25b), we obtain

$$\Gamma_R=\frac{2e^2\omega_p}{3\epsilon_\infty E_0 m_{BE}\pi}\int dq\,q^2\,\frac{\hbar/2\tau_0}{(\hbar\omega_p-E_0-\hbar^2q^2/2m_h)^2+(\hbar/2\tau_0)^2}. \tag{56d}$$

Integration over $q$ gives

$$\Gamma_R=\frac{2e^2\omega_p m_h^{3/2}}{3m_{BE}\epsilon_\infty E_0\tau_0\{[(E_0-\hbar\omega_p)^2+(\hbar/2\tau_0)^2]^{1/2}+E_0-\hbar\omega_p\}^{1/2}}. \tag{57}$$

Finally, we can write

$$\left.\frac{dn}{dt}\right|_R=\sum_{\vec{k}}\left.\frac{\partial f_{c\Gamma}}{\partial t}\right|_R=-(n_\Gamma-\bar{n}_\Gamma)\Gamma_R, \tag{58}$$

where

$$n_\Gamma=\mathcal{T}^{3/2}\rho_3(z_3), \tag{59a}$$

$$\bar{n}_\Gamma=\mathcal{T}_L^{3/2}\rho_3(z_6) \tag{59b}$$

(see Table I).

### F. Rate equations for absorption and transmission

We are now ready to derive the rate equations for describing the absorption and transmission of the excitation pulse. Let us consider the rate equation for $N(t)$ first. It can be written

$$\frac{dN}{dt}=-\alpha(t)N(t)+s(t)-l(t), \tag{60a}$$

$$\alpha(t)=\alpha_D(t)+\alpha_{FCA}(t), \tag{60b}$$

$s(t)$ is the normalized photon density per unit volume and per unit time that enters the interaction region (source)[32] and $l(t)$ is the normalized photon density per unit volume and time that leaves the interaction region.[33] We must calculate $l(t)$ in order to complete the equation above; however, we would first like to make a few remarks about (60a).

Let the excitation pulse enter the interaction region at $t=0$, and let $N(t=0)=0$. Then, the formal solution of (60a) is

$$N(t)=\int_0^t dt'\,[s(t')-l(t')]\exp\left(-\int_{t'}^{t}\alpha(t'')\,dt''\right). \tag{61}$$

Let us define

$$S(t)=\int_0^t dt'\, s(t'), \tag{62a}$$

$$L(t)=\int_0^t dt'\, l(t'). \tag{62b}$$

$S(t)$ represents the integrated photon density entering the interaction region up to the time $t$; $L(t)$ represents the integrated photon density that has left the region up to the time $t[S(0)=0, L(0)=0]$. Thus

$$N(t)=S(t)-L(t) -\left[\int_0^t dt'\, \alpha(t')\,[S(t')-L(t')] \times \exp\left(-\int_{t'}^t \alpha(t'')\,dt''\right)\right]. \tag{62c}$$

From this form it is clear that the last term on the right-hand side represents the radiation which is absorbed up to time $t$:

$$A(t)=\int_0^t dt'\, \alpha(t')[S(t')-L(t')]\exp\left(-\int_{t'}^t \alpha(t'')\,dt''\right). \tag{62d}$$

Thus

$$S(t)=A(t)+N(t)+L(t), \tag{62e}$$

which is an obvious result based on the conservation of energy. In the experiments $L \ll S$, and $L \ll A+N \sim A$. Note that $dA/dt=\alpha(t)N(t)$.

The absorption coefficient $\alpha$ is generally within the range of $10^{14}$–$10^{13}$ sec$^{-1}$. Initially we have $\alpha(t\sim 0)\sim 10^{14}$ sec$^{-1}$. Clearly, the exponential factor in (61) dominates rapidly [i.e., $\alpha(t)N(t) \gg \dot{N}(t)$], and as $N(t)$ increases from its initial zero value, it will quickly reach the asymptotic value implied by (60a):

$$N(t)=[s(t)-l(t)]/\alpha(t) \tag{63}$$

in a time of order $(1/\alpha)\sim 10^{-14}$ sec. Since the pulse width is much larger than this value, the initial rapid transient behavior of $N(t)$ can be neglected, and $N(t)$ can be taken as given by (63).

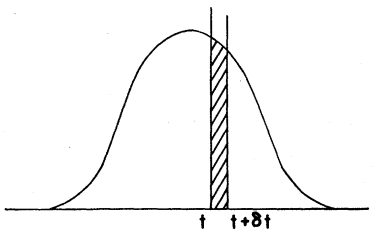


FIG. 16. Partitioning of optical pulse to calculate transmission.

In order to calculate $l(t)$, let us consider a thin slice of the pulse between $t$ and $t+\delta t$ (see Fig. 16) that has entered the crystal. The number of photons in that slice is given by $s\delta t$. The passage time of the slice is $t_p=(\epsilon_\infty)^{1/2}\mathfrak{L}/c$, where $\mathfrak{L}$ is the width of the interaction region (i.e., the crystal). $t_p \simeq 7\times 10^{-14}$ sec for $\mathfrak{L}=5.5$ $\mu$m; thus $t_p$ is much smaller than the pulse width $\bar{t}$. During the passage of the "slice of light" through the crystal, $\alpha(t)$ will not change much since $t_p \ll \bar{t}$, and $\alpha(t)$ can be considered to a good approximation as a function of $A(t)$, and

$$\frac{A(t+t_p)-A(t)}{A(t)} \simeq \frac{t_p}{A(t)}\,\frac{dA}{dt}. \tag{64a}$$

Since $dA/dt=\alpha N$, and from (63) (where we have noted that $l \ll s$) and from (62e) $A\sim S\sim st$

$$\frac{A(t+t_p)-A(t)}{A(t)} \simeq \frac{t_p s(t)}{A(t)} \sim \frac{t_p}{t} \ll 1 \tag{64b}$$

for $t_p \ll t \sim \bar{t}$. The quantity $t_p\alpha > 1$ and multiple reflections can be neglected. For this thin slice, the usual absorption equation

$$\frac{d}{dx}(\delta S)=-\left(\frac{\sqrt{\epsilon_\infty}}{c}\,\alpha\right)\delta S \tag{64c}$$

can be integrated from $x=0$ to $x=\mathfrak{L}$ and then multiplied by $(1-r)$ to account for the reflection from the back surface to obtain the density of transmitted quanta,

$$\delta L=(1-r)\delta S(x=\mathfrak{L})=(1-r)s\,\delta t e^{-t_p\alpha(t)}, \tag{64d}$$

where $r$ is the reflection coefficient. Thus

$$l(t)=(1-r)s(t)e^{-t_p\alpha(t)} \tag{65}$$

and

$$L(t)=\int_0^t dt'\,(1-r)s(t')e^{-t_p\alpha(t')}. \tag{66}$$

The transmission coefficient for the excitation pulse is given by

$$T_R^{(\mathrm{exc})}=\frac{L(\bar{t})}{S_L}=\frac{1}{S_L}\int_0^{\bar{t}} dt'\,(1-r)s(t')e^{-t_p\alpha(t')}, \tag{67}$$

where $S_L$ represents the normalized density of photons in the laser pulse ($\hbar\omega_0 N_0 S_L$ is the ratio of the laser pulse energy to the interaction volume.) Note that for a rectangular pulse of width $\bar{t}$

$$s(t)=\begin{cases}(1-r)S_L/\bar{t} & \text{for } 0\le t\le \bar{t},\\ 0 & \text{for } \bar{t}<t,\end{cases} \tag{68}$$

where $(1-r)$ in front of $S_L$ accounts for the reflection from the front surface of the sample, and thus

$$T_R^{(\mathrm{exc})} = \frac{1}{\bar{t}} \int_0^{\bar{t}} dt' \, (1-\gamma)^2 e^{-t_p \alpha(t')}. \tag{69}$$

The reflection coefficient was experimentally measured for all intensities of the laser beam used in the experiment, and was found to be nearly constant.[34] It is given by

$$\gamma = (\sqrt{\epsilon_\infty} - 1)^2/(\sqrt{\epsilon_\infty} + 1)^2 = 0.36. \tag{70}$$

In order to collect together our working equations, we substitute the results given by equations (26), (58), and (63) in (10) and obtain

$$\gamma_\epsilon(t) \frac{d\epsilon}{dt} + \gamma_{\mathcal{T}}(t) \frac{d\mathcal{T}}{dt} = \frac{\alpha_D}{\alpha}(s-l) - (n_\Gamma - \bar{n}_\Gamma)\Gamma_R. \tag{71a}$$

Likewise we substitute (27), (40), (45), and (63) in (20) in order to obtain

$$\gamma_{u\epsilon}(t) \frac{d\epsilon}{dt} + \gamma_{u\mathcal{T}}(t) \frac{d\mathcal{T}}{dt}$$

$$= \frac{\alpha_D}{\alpha}(s-l) + \frac{\alpha_{\mathrm{FCA}}}{\alpha}(s-l) - [\Gamma_0(t) + \Gamma_A(t)]. \tag{71b}$$

Solving (71a) and (71b) for $d\epsilon/dt$ and $d\mathcal{T}/dt$, taking $dh/dt$ from (13), $d\mathcal{T}_L/dt$ from (50) and $l(t)$ from (65) we have our complete set of working equations:

$$\frac{d\epsilon}{dt} = \left(\frac{\gamma_{u\mathcal{T}}}{\Delta}\right)\left(\frac{\alpha_D}{\alpha}\right)(s-l) - \left(\frac{\gamma_{u\mathcal{T}}}{\Delta}\right)(n_\Gamma - \bar{n}_\Gamma)\Gamma_R$$

$$- \left(\frac{\gamma_{\mathcal{T}}}{\Delta}\right)(s - l - \Gamma_0 - \Gamma_A), \tag{72a}$$

$$\frac{d\mathcal{T}}{dt} = -\left(\frac{\gamma_{u\epsilon}}{\Delta}\right)\left(\frac{\alpha_D}{\alpha}\right)(s-l) + \left(\frac{\gamma_{u\epsilon}}{\Delta}\right)(n_\Gamma - \bar{n}_\Gamma)\Gamma_R$$

$$+ \left(\frac{\gamma_\epsilon}{\Delta}\right)(s - l - \Gamma_0 - \Gamma_A), \tag{72b}$$

$$\frac{dh}{dt} = -\gamma_{\epsilon h} \frac{d\epsilon}{dt} + \gamma_{\mathcal{T}h} \frac{d\mathcal{T}}{dt}, \tag{72c}$$

$$\frac{d\mathcal{T}_L}{dt} = \frac{1}{c_L}(\Gamma_0 + \Gamma_A), \tag{72d}$$

$$l(t) = (1-\gamma)s(t)e^{-t_p \alpha(t)}, \tag{72e}$$

where

$$\Delta(t) \equiv \gamma_{u\mathcal{T}}(t)\gamma_\epsilon(t) - \gamma_{u\epsilon}(t)\gamma_{\mathcal{T}}(t)$$

$$= \{\mathcal{T}^2/4[\rho_1(z_1) - \sigma_2(z_2)]\}$$

$$\times \{10[\nu_1(z_1) + \nu_2(z_2)][\rho_1(z_1) - \sigma_1(z_1)][\rho_1(z_1) - \sigma_2(z_2)]$$

$$- 9[\rho_1(z_1)]^2[2\rho_1(z_1) - \sigma_1(z_1) - \sigma_2(z_2)]\}. \tag{72f}$$

Given $s(t)$ and $\epsilon(0)$, $h(0)$, $\mathcal{T}(0)$, $\mathcal{T}_L(0)$, these equations can be solved numerically for $\epsilon(t)$, $h(t)$, $\mathcal{T}(t)$, $\mathcal{T}_L(t)$, and $l(t)$ (or $L$).

### G. Integration of dynamical equations

We now make a few qualitative remarks about (72a)–(72e) and present their numerical solutions. At the initial phase of the excitation pulse absorption, $\mathcal{T}$ increases quite rapidly compared to $n$ since after a direct optical transition an electron in the $\Gamma$ valley scatters to one of the $L$-$X$ valleys. After such a scattering event an energy of approximately $1 - \mathcal{E}_G$ goes into electronic thermal agitation. Therefore, $\mathcal{T}$ approaches[35] $\frac{1}{3}(1 - \mathcal{E}_G)$ (~1500 °K) rapidly and $\epsilon$ decreases to a negative value. In this initial phase, plasmon recombination, phonon relaxation and free-carrier absorption terms are completely neglibible; thus, we may apply a nondegenerate (high temperature) approximation to the integrals in the $\gamma$ coefficients (see Table II). After this initial state, $\mathcal{T}$ may decrease or increase depending upon the comparative rates of the phonon relaxation, plasmon recombination, and the free-carrier absorption.

As $n$ increases, initially the transmission also increases. Eventually if $n$ is sufficiently large, plasma recombinations begin to compete with direct absorptions and $n$ begins to saturate. The saturation region is reached when

$$(\alpha_D/\alpha)s \sim (n_\Gamma - \bar{n}_\Gamma)\Gamma_R. \tag{73a}$$

This corresponds to $dn/dt \sim 0$. In this region, those electrons which have just made direct optical transitions can recombine with holes via emission of plasmons and become available again for direct absorption. Plasmons rapidly decay and transfer their energy to electrons and holes. Thus, in the saturation region, the main result of direct absorption is the heating of electrons and holes.

TABLE II. High-temperature approximation (low densities).

| |
|---|
| $F(x) \to e^{-x}$ |
| $\rho_i(z) \to \frac{1}{2}\sqrt{\pi}\, A_i e^{-z}$ |
| $\sigma_i(z) \to (\sqrt{\pi}/4\sqrt{2}) A_i e^{-2z}$ |
| $\nu_i(z) \to \frac{3}{4}\sqrt{\pi}\, A_i e^{-z}$ |
| $n \to \frac{1}{2}\sqrt{\pi}\, A_1 \mathcal{T}^{3/2} e^{-z_1} = (\sqrt{\pi}/2) A_2 \mathcal{T}^{3/2} e^{-z_2}$ |
| $\gamma_\epsilon \to n/\mathcal{T}$ |
| $\gamma_{\mathcal{T}} \to (n/\mathcal{T})(1.5 - z_1) \approx -(nz_1/\mathcal{T})$ |
| $\gamma_{\epsilon h} \to 1$ |
| $\gamma_{\mathcal{T}h} \to z_2 - z_1$ |
| $\gamma_{u\epsilon} \to (n/\mathcal{T})(\mathcal{E}_G + 3\mathcal{T})$ |
| $\gamma_{u\mathcal{T}} \to (n/\mathcal{T})[(1.5 + z_1)\mathcal{E}_G + 3\mathcal{T}(2.5 + z_1)] \approx (nz_1/\mathcal{T})(\mathcal{E}_G + 3\mathcal{T})$ |
| $\Delta \to 3n^2/\mathcal{T}$ |

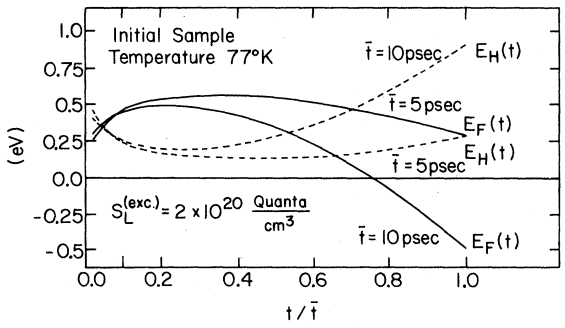


FIG. 17. Temporal behavior of Fermi energies during passage of excitation pulse.

In this region, $\mathcal{T}$ then varies according to

$$\frac{d\mathcal{T}}{dt} \sim \frac{\gamma_\epsilon}{\Delta}(s - \Gamma_0 - \Gamma_A) \tag{73b}$$

and increases rather rapidly. In the saturation region, the trajectories of the system remain close to the constant $n$ curves in Fig. 10.

The following several figures present the results of numerically integrating (72a)–(72e) during the period the excitation pulse is present in the sample. All numerical solutions have been generated assuming a rectangular optical pulse of width $\bar{t}$. Figures 17 and 18 illustrate the temporal evolution of the Fermi energies of the electrons and holes and of the carrier temperature as an excitation pulse of constant energy traverses the sample. We have presented these curves for several different pulse widths to emphasize that the pulse width has a significant influence on the temporal evolution of these quantities. Note that for the large excitation pulse energy used in these figures the temperature begins near 1500 °K and

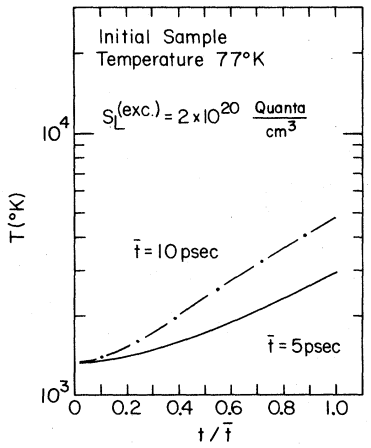


FIG. 18. Temporal behavior of electron-hole temperature.

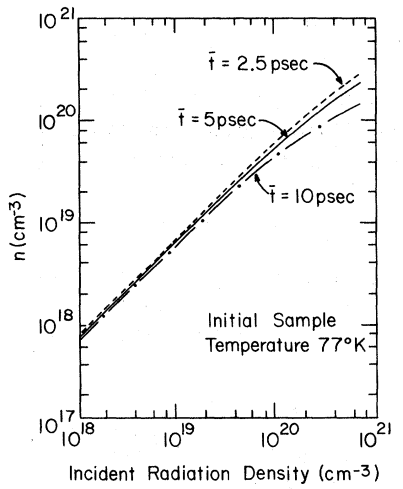


FIG. 19. Electron density vs excitation pulse density for different pulse widths and initial lattice temperature of 77 °K.

rises due to plasmon recombinations as discussed above.

Figures 19–24 show the final carrier number, carrier temperature, and lattice temperature immediately after the passage of the excitation pulse as a function of excitation pulse energy for lattice temperatures of 77 and 297 °K. Again the dependence of these curves on pulse width is emphasized. Notice that, due to plasmon emission, the electron number begins to saturate somewhat and the carrier temperature is elevated for large excitation pulse energies as discussed earlier. Also note that this model does not provide for sufficient lattice heating to account for the surface damage

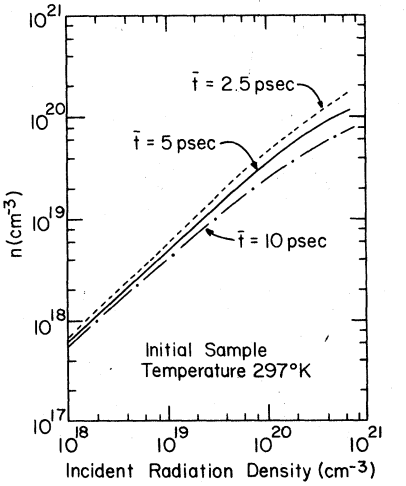


FIG. 20. Electron density vs excitation pulse density for different pulse widths and initial lattice temperature of 297 °K.

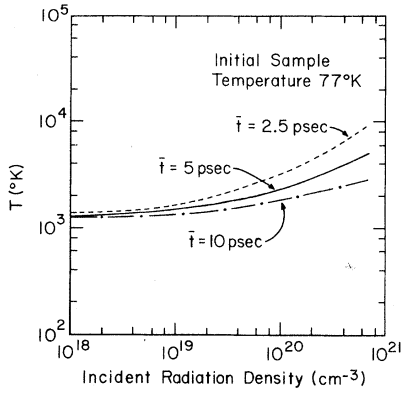


FIG. 21. Electron-hole temperature vs excitation pulse density for different pulse widths and initial lattice temperature of 77 °K.

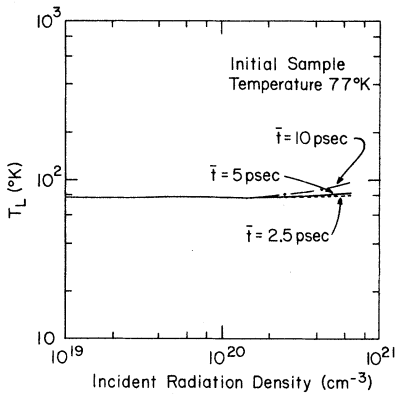


FIG. 23. Lattice temperature vs excitation pulse density for different pulse widths and initial lattice temperature of 77 °K.

we observe at the largest pulse energies. In Figs. 25 and 26, we show the corresponding single pulse, or excitation pulse, transmission. These curves are presented as a function of pulse width for lattice temperatures of 77 and 300 °K.

For $t>\bar{t}$, we set $s=0, l=0$. The system begins to evolve according to

$$\frac{d\epsilon}{dt}=\left(\frac{\gamma_T}{\Delta}\right)(\Gamma_0+\Gamma_A), \tag{74a}$$

$$\frac{dT}{dt}=-\left(\frac{\gamma_\epsilon}{\Delta}\right)(\Gamma_0+\Gamma_A). \tag{74b}$$

$dT_L/dt$ and $dh/dt$ are still given by (72c) and (72d). In (74a) and (74b) we have omitted the plasmon-assisted recombinations since, as discussed previously, when the excitation pulse is turned off the plasmon process is likewise rapidly turned off. Notice that in the experiment the largest probe pulse delay was about 300 psec and that direct and indirect optical recombinations are still negligible for such delay times. Since the experimental probe pulse intensities were small compared to the excitation pulse intensities, the system evolves according to (74a) and (74b) and (72c) and (72d) when the probe pulse passes through the interaction region, rather than (72a) and (72b) with $s=s_{\text{probe}}, l=l_{\text{probe}}$.

For a rectangular pulse of width $\bar{t}$, the probe transmission is given by

$$L_{\text{probe}}=\int dt'\,(1-r)s_{\text{probe}}(t')e^{-t_p\alpha(t')} \tag{75}$$

and the transmission coefficient by

$$T_R^{\text{probe}}=\frac{(1-r)^2}{\bar{t}}\int_{t_d-\bar{t}/2}^{t_d+\bar{t}/2}dt'\,e^{-t_p\alpha(t')}, \tag{76}$$

where $t_d$ is the delay time of the probe with respect to the excitation pulse. For $t_d>\bar{t}$, $T_R^{\text{probe}}$ increases at first due to electron-hole relaxation. As electrons and holes relax via phonon emissions, they clog the optically coupled states $E'$ and $E''$ in Fig.

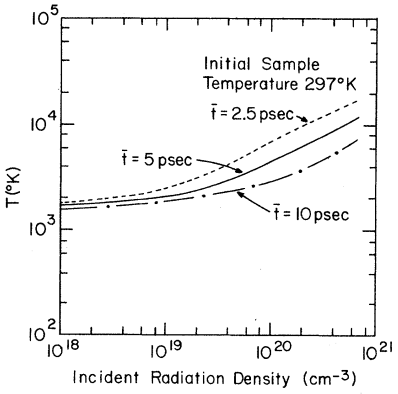


FIG. 22. Electron-hole temperature vs excitation pulse density for different pulse widths and initial lattice temperature of 297 °K.

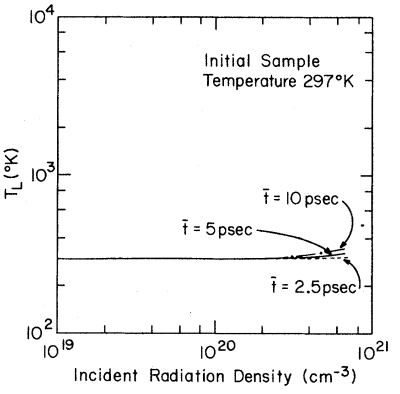


FIG. 24. Lattice temperature vs excitation pulse density for different pulse widths and initial lattice temperature of 297 °K.

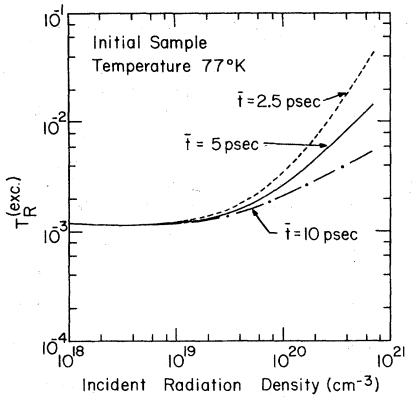


FIG. 25. Excitation pulse transmission vs excitation pulse density for initial lattice temperature of 77 °K.

5 and reduce absorption. Further relaxation can eventually free these states for optical transitions, and probe transmission can decrease. These ideas are summarized in Fig. 7. Figures 27 and 28 show probe transmission versus delay time for different excitation pulse radiation densities and for the two initial sample temperatures 77 and 297 °K. For these solutions, the pulse width is assumed to be 5 psec. As the excitation pulse intensity decreases, the probe transmission curve is generally lowered.[36]

### III. COMPARISON WITH EXPERIMENTAL DATA AND CONCLUSIONS

The experimental data and the theoretical curves for the excitation pulse transmission are shown in Fig. 29. The theoretical curves are for a 5-psec pulse width and a $3 \times 10^{-7}$-cm$^3$ interaction volume. This volume corresponds to a focused spot diameter that is in accord with the experimentally estimated value of about 250 $\mu$m. The agreement

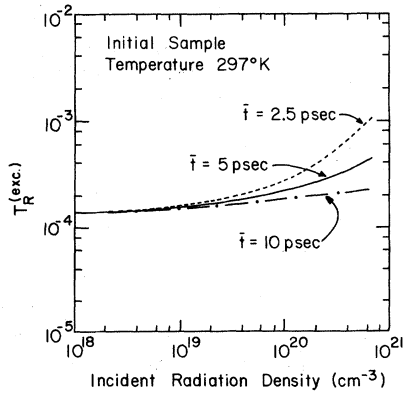


FIG. 26. Excitation pulse transmission vs excitation pulse density for initial temperature of 297 °K.

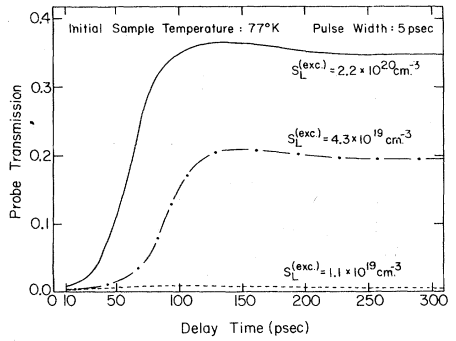


FIG. 27. Probe transmission vs delay time for different excitation pulse densities and initial lattice temperature of 77 °K.

between data and theory is good at lower excitation energies. At the extremely high excitation energies ($\sim 4 \times 10^{14}$ quanta) the theoretical enhanced transmission does not saturate as does the experimental transmission. However, since we are uncertain whether the saturation in experimental transmission is due to bulk effects or due to the onset of surface damage, we shall not dwell on this point.

Figure 30 shows the probe transmission data (minus the zero delay time spike) and the corresponding theoretical curves. The theoretical curves were generated for $2 \times 10^{20}$-cm$^{-3}$ incident excitation quanta density, 5-psec pulse width, and $10^{-6}$-cm$^3$ interaction volume. The agreement between the theory and the experimental data is reasonable for both 77 and 297 °K.

The overall good agreement between the theory and the experiment permits us to draw a number of conclusions. An important assumption in our calculations was that the large number of free carriers created by the excitation pulses be described by Fermi-like distributions. Apparently, this assumption works quite well despite the in-

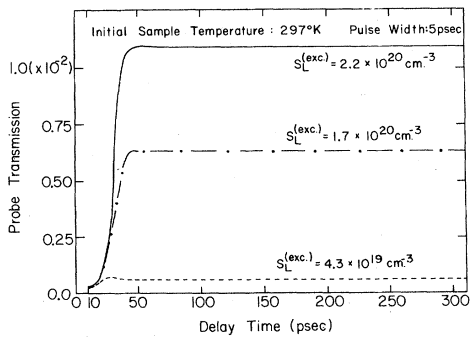


FIG. 28. Probe transmission vs delay time for different excitation pulse densities and initial lattice temperature of 297 °K.

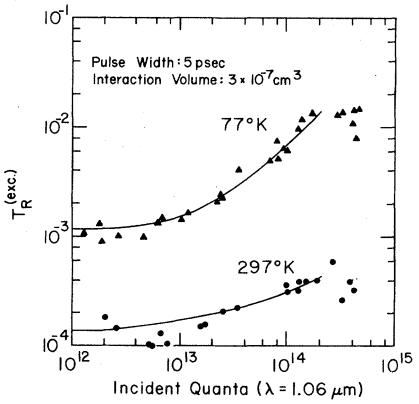


FIG. 29. Theoretical and experimental excitation pulse transmission vs excitation pulse intensity.

tensity and the short duration of the optical pulses. Clearly, in order to observe a large deviation from a Fermi-like distribution in a thin sample, one must go to even shorter pulse widths than those achieved in these experiments. It also appears that if the sample is only a few micrometers thick, then one can average over the spatial effects and obtain good results.

Many-body (plasmon) effects are extremely important in intense nonlinear light absorption owing to the large number of carriers created and the short lifetime of the optically coupled states. Plasmon-assisted recombinations play a role in the behavior of both excitation and probe transmission by saturating the free carrier densities while increasing their temperature. Plasmon-assisted recombinations should have observable consequences in similar experiments with other materials. How they would affect the excitation and probe transmission would depend on the particulars of the energy-band structure of each semiconductor.

Let us emphasize again that the highest plasma

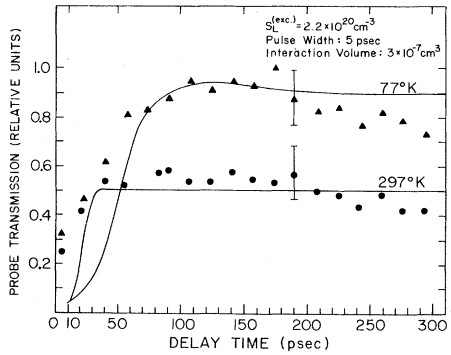


FIG. 30. Theoretical and experimental probe transmission vs delay time.

frequencies achieved in the experiments are actually less than $E_0/2\hbar$. The maximum electron densities occurring in the vicinity of $2\times10^{20}$ cm$^{-3}$, which corresponds to $(\max\omega_p)/\omega_0 \simeq 0.3$. There is a directly observable quantity, namely the refractive index for the optical frequency $\omega_0$, which is directly related to the ratio $\omega_p/\omega_0$. For the electron density quoted above, the maximum change in the refractive index divided by the initial refractive index is given by[37]

$$\max\left(\frac{\Delta_{\text{ref index}}}{\text{ref index}}\right) \simeq -\frac{1}{2}\left(\frac{\max\omega_p}{\omega_0}\right)^2 \simeq -0.05.$$

This is in good agreement with the direct measurements of the refractive index.[4]

In Sec. II, the role of the phonon-assisted relaxation was discussed in detail. We have seen that the reason the relaxation extends over a time span of a hundred picoseconds is due to the fact that the phonon-assisted relaxation in Ge is strongly dependent on the difference between the temperatures of the free carriers and the lattice and due to the existence of conduction band valleys in Ge. In different materials with different energy-band structures and electron-phonon coupling constants, the behavior of the probe pulse transmission would be (and is) drastically different.

As mentioned earlier, the lattice temperature increase is generally small. Here, "small" can mean as much as 10–30 °K at large light intensities. This may be sufficiently large to be experimentally measurable.

An important assumption in the calculation of the phonon-assisted relaxation rates was the fact that phonon distributions were given by the usual Bose distributions. This assumption apparently works well. However, at large intensities (near $10^{15}$ laser quanta), large numbers of phonons are generated. It is quite possible that a phonon instability may occur, i.e., the number of quanta in some phonon modes may grow to larger values than those given by equilibrium values. This should be investigated in the future.

An interesting feature of the theoretical model as developed is the behavior of the transmission for different pulse widths. One can see from Figs. 25 and 26 that transmission changes significantly near the saturation region when pulse width is increased. Since it is possible to split an optical pulse into separate parts and then rejoin them, it is possible to perform the experiments with variable duration pulses. These and other experiments are currently under way.

## ACKNOWLEDGMENTS

We thank F. Hopf for his valuable criticisms, W. P. Latham and R. J. McCarthy for their aid in

computer programming, and J. Bessey, R. Emrick, R. Parmenter, B. O. Seraphin, R. Stark, H. van Driel, and R. Young for helpful comments concerning the manuscript.

## APPENDIX A: $\Gamma \rightarrow L,X$ TRANSITIONS VIA PHONON EMISSIONS

Let us consider a particular side valley, say (111) valley. Using the electron-phonon coupling Hamiltonian given by (35), the transition rate for an electron going from the $\Gamma$ valley to the (111) valley via spontaneous emission of optical and acoustical phonons can be written

$$R(k)=\left(\frac{2\pi}{\hbar}\right)\sum_{\vec{q}',\mu}\left(\frac{\hbar}{2\rho\Omega_{\mu q'}}\right)\times|Q_\mu(q')|^2|\langle c,\vec{k}-\vec{q}'|e^{-i\vec{q}'\cdot\vec{r}}|c,\vec{k}\rangle|^2\times\delta(E_c(\vec{k})-E_c(\vec{k}-\vec{q}')-\hbar\Omega_{\mu q'}). \quad \text{(A1a)}$$

where $\vec{k}$ is sufficiently small such that $|c,\vec{k}\rangle$ refers to an electron in the $\Gamma$ valley and $-\vec{q}'$ is sufficiently large and generally pointing in [111] direction such that $|c,\vec{k}-\vec{q}'\rangle$ refers to an electron in the [111] valley. If we let $\vec{k}_{[111]}$ represent the wave vector of the lowest point (in energy) of the [111] valley, then $q' \sim k_{[111]}$, and $q' \gg k$. Since $q'$ is smaller than the reciprocal-lattice vector, $|\langle c,\vec{k}-\vec{q}'|e^{-i\vec{q}'\cdot r}|c,\vec{k}\rangle|^2 \approx 1$. Electron-phonon coupling parameters $Q_\mu(\vec{q}')$ were discussed in the text. For optical phonons $Q_{LO}=Q_0\cos\phi$ and $Q_{TO}=Q_0\sin\phi$, where $\phi$ is the angle between $-\vec{q}'$ and $\vec{k}_{(111)}$. Since $-\vec{q}'$ is assumed to be generally in the direction of $\vec{k}_{(111)}$, $Q_{LO}\approx Q_0$ and $Q_{TO}\approx 0$. Thus for optical phonons the right-hand side of (A1a) becomes

$$\frac{\pi Q_0^2}{\rho\Omega_0}\sum_{\vec{q}'}\delta(E_c(\vec{k})-E_c(\vec{k}-\vec{q}')-\hbar\Omega_0). \quad \text{(A1b)}$$

For acoustical phonons, $Q_{LA}=q'(\Lambda_d+\Lambda_u\cos^2\phi)\approx q'(\Lambda_d+\Lambda_u)$ and $Q_{TA}=-q'\Lambda_u\cos\phi\sin\phi\approx 0$. Since $q'\approx k_{[111]}$, $Q_{LA}\approx k_{[111]}(\Lambda_d+\Lambda_u)\equiv Q_A$. Also, $c_A q'\approx c_A k_{[111]}\approx\Omega_0$.[26] Therefore, we obtain the contribution of both optical and acoustical phonons

$$R(k)\underset{\Gamma\rightarrow[111]}{\sim}\frac{\pi(Q_0^2+Q_A^2)}{\rho\Omega_0}\sum_{q'}\delta(E_c(\vec{k})-E_c(\vec{k}-\vec{q}')-\hbar\Omega_0). \quad \text{(A1c)}$$

In our approximate band model, the electron energies are given by

$$E_c(\vec{k})=E_0+\hbar^2k^2/2m_0 \quad \text{(A1d)}$$

and

$$E_c(\vec{k}-\vec{q})=E_G+[\hbar^2(\vec{k}-\vec{q}'-\vec{k}_{[111]})^2]/2m_c. \quad \text{(A1e)}$$

The phonon energy in the $\delta$ function can be neglected, since it is quite small compared to electron energies. Letting $-\vec{q}'=\vec{k}_{[111]}+\vec{q}''$, where $q''\ll q', k_{[111]}$, the integral over the $\delta$ function is trivial, and yields

$$R(k)\underset{\Gamma\rightarrow(111)}{\sim}\frac{(2m_c)^{3/2}(Q_0^2+Q_A^2)}{4\pi\rho\Omega_0\hbar^3}\left(E_0+\frac{\hbar^2k^2}{2m_0}-E_G\right)^{1/2}. \quad \text{(A2)}$$

For an electron just raised to the $\Gamma$ valley by optical transition $E_0+h^2k^2/2m_0\simeq\hbar\omega_0$. Thus, summing over all valleys, we obtain

$$\frac{1}{\tau_0}=\sum_j R_{\Gamma\rightarrow j}\simeq\frac{5(Q_0^2+Q_A^2)(2m_c)^{3/2}}{2\pi\rho\Omega_0\hbar^3}(\hbar\omega_0-E_G)^{1/2}. \quad \text{(A3)}$$

For $m_c=0.22m$, $\hbar\omega_0=1.17$ eV, $E_G\simeq 0.7$ eV, $\rho\simeq 5.3$ g/cm$^3$, $\hbar\Omega_0\simeq 0.02$ eV, $Q_0\simeq 6\times10^{-4}$ erg/cm, and $Q_A\simeq 2\times10^{-3}$ erg/cm, $1/\tau_0\simeq 1\times10^{14}$ sec$^{-1}\geq$ (the absorption rate).

## APPENDIX B: COULOMB THERMALIZATION

In this appendix we will calculate the lifetime of an occupied state, which is finite due to Coulomb scatterings among electrons and holes if the distributions are not Fermi-like. For the sake of simplicity, we will neglect the long-wavelength screening of the Coulomb fields. For an electron state $\vec{k}$ in the $i$th valley, the scattering rate out of the state $\vec{k}$ is given by

$$\Gamma_{\vec{k}}^{\text{out}}=\left(\frac{2\pi}{\hbar}\right)\int\frac{2d\vec{k}'}{(2\pi)^3}\int\frac{d\vec{q}}{(2\pi)^3}\left(\frac{4\pi e^2}{q^2\epsilon_\infty}\right)^2[1-f_{ci}(\vec{k}-\vec{q})]\times\left(\sum_j f_{cj}(\vec{k}')[1-f_{cj}(\vec{k}'+\vec{q})]\delta(E_{ci}(\vec{k}-\vec{q})-E_{ci}(\vec{k})+E_{cj}(\vec{k}'+\vec{q})-E_{cj}(\vec{k}'))\right.$$
$$\left.+\sum_v[1-f_{hv}(\vec{k}')]f_{hv}(\vec{k}'+\vec{q})\delta(E_{ci}(\vec{k}-\vec{q})-E_{ci}(\vec{k})-E_{hv}(\vec{k}'+\vec{q})+E_{hv}(\vec{k}'))\right). \quad \text{(B1)}$$

$j$ varies over the conduction-band valleys, $v$ over the two valence bands. $f_{cj}$ and $f_{hv}$ are electron and hole distributions, respectively; $E_{cj}$ and $E_{hv}$ are electron and hole energies ($E_{hv}$ is positive).

The scattering rate into the state $\vec{k}$ is given by

$$\Gamma_{\vec{k}}^{\text{in}}=\left(\frac{2\pi}{\hbar}\right)\int\frac{2d^3\vec{k}'}{(2\pi)^3}\int\frac{d^3\vec{q}}{(2\pi)^3}\left(\frac{4\pi e^2}{q^2\epsilon_\infty}\right)f_{ci}(\vec{k}-\vec{q})$$
$$\times\left(\sum_j[1-f_{cj}(\vec{k}')]f_{cj}(\vec{k}'+\vec{q})\delta(E_{ci}(k-q)-E_{ci}(k)+E_{cj}(k'+q)-E_{cj}(k'))\right.$$
$$\left.+\sum_v[1-f_{hv}(\vec{k}'+\vec{q})]f_{hv}(\vec{k}')\delta(E_{ci}(\vec{k}-\vec{q})-E_{ci}(\vec{k})-E_{hv}(\vec{k}'+\vec{q})+E_{hv}(\vec{k}'))\right). \tag{B2}$$

Of course, if the distributions are Fermi-like, with a common temperature for electrons and holes, then $\Gamma_{\vec{k}}^{\text{in}}=\Gamma_{\vec{k}}^{\text{out}}$, for any state $\vec{k}$. We will evaluate $\Gamma$'s for two kinds of rather simple distributions which are energy dependent only. To simplify the algebra, we will take the effective masses of electrons and holes to be the same $m^*$ (since $m_c\simeq 0.22m, m_h\simeq 0.34m$, this is not too drastic). Also, the total electron density is always taken to be equal to the total hole density.

(a) Let the distributions be Lorentzian with narrow widths, such that

$$f_{cj}(k)=\Delta^2/\{[E_{cj}(\vec{k})-E_G-\tilde{E}]^2+\Delta^2\}$$
$$\simeq\pi\Delta\delta(E_{cj}(\vec{k})-E_G-\tilde{E}), \tag{B3a}$$

$$f_{hv}(k)=(5\Delta)^2/\{[E_{hv}(\vec{k})-\tilde{E}]^2+(5\Delta)^2\}$$
$$\simeq 5\pi\Delta\delta(E_{hv}(\vec{k})-\tilde{E}), \tag{B3b}$$

i.e., $\delta\equiv\Delta/\tilde{E}\ll 1$.

(i) Let us consider an occupied state $\vec{k}$: $E_{ci}(k)=\tilde{E}+E_G$. Then,

$$\Gamma_{\vec{k}}^{\text{in}}=0, \tag{B4a}$$

$$\Gamma_{\vec{k}}^{\text{out}}=(160e^4m^*/3\hbar^3\epsilon_\infty^2)(1-\delta)^{3/2}/\delta. \tag{B4b}$$

(ii) For the states $\vec{k}'$ such that $E_{ci}(\vec{k}')<\tilde{E}+E_G-\Delta$ or $E_{ci}(\vec{k}')>\tilde{E}+E_G+\Delta$,

$$\Gamma_{\vec{k}'}^{\text{in}}=(80e^4m^*/3\hbar^3\epsilon_\infty^2)(1-\delta)^{3/2}/\delta, \tag{B5a}$$

$$\Gamma_{\vec{k}'}^{\text{out}}=0. \tag{B5b}$$

Setting $m^*\simeq 0.22m, \epsilon_\infty=16$, we find $80e^4m^*/3\hbar^3\epsilon_\infty^2\simeq 10^{15}$ sec$^{-1}$. Thus $\Gamma_k^{\text{out}}, \Gamma_{k'}^{\text{in}}\gg$ (light absorption rate).

(b) Let the distributions be of the following form:

$$f_c(\vec{k})=\begin{cases}1 \text{ if } \hbar^2(K-\frac{1}{2}\Delta)^2/2m^*<E_c(\vec{k})-E_G\\ <\hbar^2(K+\frac{1}{2}\Delta)^2/2m^*,\\ 0 \text{ elsewhere;}\end{cases} \tag{B6a}$$

$$f_h(\vec{k})=\begin{cases}1 \text{ if } \hbar^2(K-\frac{1}{2}\Delta)^2/2m^*<E_h(\vec{k})\\ <\hbar^2(K+\frac{1}{2}\Delta)^2/2m^*,\\ 0 \text{ elsewhere;}\end{cases} \tag{B6b}$$

and $2.5\Delta<K<(1.5+\sqrt{2})\Delta$ (i.e., the width $\Delta$ is large).

Let us consider an occupied electron state $\vec{k}$ in the $i$th valley. The contribution of the conduction-band electrons to the $\Gamma_k^{\text{out}}$ is given by

$$\Gamma_k^{\text{out}(c)}=(5e^4m^*/\pi\hbar^3\epsilon_\infty^2)I(k,K_-), \tag{B7a}$$

where

$$K_-=K-\tfrac{1}{2}\Delta, \tag{B7b}$$

$$I(k,K_-)=4\ln\left(\frac{k+K_-}{k-K_-}\right)-2\frac{K_-}{k}+\frac{2K_-(k^4+K_-^4)(k^2+\frac{1}{3}K_-^2)}{k(k^2-K_-^2)^3}$$
$$+\frac{8kK_-^2}{(k^2-K_-^2)^2}+\frac{4K_-^3-8k^2K_-}{k(k^2-K_-^2)}. \tag{B7c}$$

Let $k=K_-+\delta$. As $\delta\to 0$,

$$I(k,K_-)\simeq 4\ln(4K_-/\delta)+\tfrac{5}{6}(K_-/\delta)^3+O(1/\delta^2)\to\infty. \tag{B8}$$

For $k=K+\frac{1}{2}\Delta$,

$$I\simeq 16 \text{ if } K=2.5\Delta, \tag{B9a}$$

$$I\simeq 26 \text{ if } K=2.9\Delta. \tag{B9b}$$

Thus, $\Gamma_k^{\text{out}(c)}\gtrsim 80e^4m^*/\pi\hbar^3\epsilon_\infty^2\simeq 3\times 10^{14}$ sec$^{-1}$. The contribution of the holes is about the same; thus $\Gamma_k^{\text{out}}\gtrsim 6\times 10^{14}$ sec$^{-1}$ which is greater than the absorption rate. Finally, we note that when we include further screening effects this rate drops to around $10^{13}$ sec$^{-1}$.

## APPENDIX C: RADIATION ABSORPTION RATES

(a) *Direct absorptions.* From the diagrams shown in Fig. 8, we readily find

$$\left.\frac{\partial N_{\lambda\vec{q}}^{(\mathrm{rad})}}{\partial t}\right|_{\mathrm{DA}} = -2\left(\frac{2\pi}{\hbar}\right)\left(\frac{e}{mc}\right)^2\left(\frac{2\pi c^2\hbar}{\epsilon_\infty\omega_q}\right)N_{\lambda\vec{q}}^{(\mathrm{rad})}$$
$$\times\sum_{\vec{k}}|\langle c\Gamma,\vec{k}+\vec{q}|\,e^{i\vec{q}\cdot\vec{r}}\hat{\xi}_\lambda(\vec{q})\cdot\vec{p}\,|v,\vec{k}\rangle|^2\,[1-f_H(\vec{k})][1-f_{c\Gamma}(\vec{k}+\vec{q})]\delta(E_{c\Gamma}(\vec{k}+\vec{q})+E_H(\vec{k})-\hbar\omega_q)$$
$$+2\left(\frac{2\pi}{\hbar}\right)\left(\frac{e}{mc}\right)^2\left(\frac{2\pi c^2\hbar}{\epsilon_\infty\omega_q}\right)(N_{\lambda\vec{q}}^{(\mathrm{rad})}+1)\sum_{\vec{k}}|\langle v,\vec{k}|\,e^{-i\vec{q}\cdot\vec{r}}\hat{\xi}_\lambda(\vec{q})\cdot\vec{p}\,|c\Gamma,\vec{k}+\vec{q}\rangle|^2 f_{c\Gamma}(\vec{k}+\vec{q})f_H(\vec{k})\delta(E_{c\Gamma}(\vec{k}+\vec{q})$$
$$+E_H(\vec{k})-\hbar\omega_q). \tag{C1}$$

Here, $\hat{\xi}_\lambda(\vec{q})$ denotes photon polarization. The meaning of the other symbols are as defined in the text. The sum $\sum_{\vec{k}}$ also includes spin summation. The extra factor of 2 in front of the terms is due to the fact that we have two degenerate valence bands. The photon momenta are completely negligible compared to the electron and hole momenta. Therefore, $q$'s in the interband matrix element of $\vec{p}$, in $f$'s and in the $\delta$ functions can be omitted. Also, the radiation is primarily at the circular frequency $\omega_0$ and the corresponding $N^{(\mathrm{rad})} \gg 1$. Therefore, the spontaneous emission term can be neglected. To obtain

$$\left.\frac{\partial N}{\partial t}\right|_{\mathrm{DA}} = \frac{1}{N_0}\sum_{\lambda\vec{q}}\left.\frac{\partial N_{\lambda\vec{q}}^{(\mathrm{rad})}}{\partial t}\right|_{\mathrm{DA}},$$

we perform $\sum_{\lambda\vec{q}}$ on (C1), and find

$$\left.\frac{\partial N}{\partial t}\right|_{\mathrm{DA}} = -\left(\frac{8\pi^2e^2}{3m^2\epsilon_\infty\omega_0}\right)N(t)\int\frac{2d^3\vec{k}}{(2\pi)^3}|\langle c\Gamma,\vec{k}|\,\vec{p}\,|v,\vec{k}\rangle|^2[1-f_{c\Gamma}(\vec{k})-f_H(\vec{k})]\delta(E_{c\Gamma}(\vec{k})+E_H(\vec{k})-\hbar\omega_0). \tag{C2}$$

The interband matrix element of $\vec{p}$ near the $\Gamma$-valley band edge is given by

$$|\langle c\Gamma,\vec{k}|\,\vec{p}\,|v,\vec{k}\rangle|^2 \simeq m^2E_0(m_0+m_h)/2m_0m_h. \tag{C3}$$

In our approximate band structure, the electron and hole energies are given by

$$E_{c\Gamma}(\vec{k}) = E_0+\hbar^2k^2/2m_0, \quad E_H(\vec{k}) = \hbar^2k^2/2m_h. \tag{C4}$$

The integral over the $\delta$ function is trivial, and yields

$$\left.\frac{\partial N}{\partial t}\right|_{\mathrm{DA}} = -N(t)\left(\frac{4e^2E_0}{3\epsilon_\infty\hbar^2\omega_0}\right)\left(\frac{2m_0m_h(\hbar\omega_0-E_0)}{\hbar^2(m_0+m_h)}\right)^{1/2}$$
$$\times\left(1-\left\{1+\exp\left[\beta\left(\frac{m_0}{m_0+m_h}(\hbar\omega_0-E_0)+E_H\right)\right]\right\}^{-1}-\left\{1+\exp\left[\beta\left(E_0+\frac{m_h}{m_0+m_h}(\hbar\omega_0-E_0)-E_F\right)\right]\right\}^{-1}\right), \tag{C5}$$

$$\left.\frac{\partial N}{\partial t}\right|_{\mathrm{DA}} = -N(t)\alpha_0[1-F(z_4)-F(z_5)]$$
$$= -N(t)\alpha_D(t). \tag{28}$$

To find

$$\left.\frac{\partial n}{\partial t}\right|_{\mathrm{DA}} = \frac{1}{N_0}\int\frac{2d^3\vec{k}}{(2\pi)^3}\left.\frac{\partial f_{c\Gamma}(\vec{k})}{\partial t}\right|_{\mathrm{DA}}, \quad \left.\frac{\partial f_{c\Gamma}(\vec{k})}{\partial t}\right|_{\mathrm{DA}}$$

can be calculated in completely analogous manner. It is given by the negative of the righthand side of (C1) if $\sum_{\vec{k}}$ is replaced by $\sum_{\lambda\vec{q}}$. Thus, $\partial n/\partial t|_{\mathrm{DA}}$ is given by the negative of the right-hand side of (C2), and

$$\left.\frac{\partial n}{\partial t}\right|_{\mathrm{DA}} = N(t)\alpha_0[1-F(z_4)-F(z_5)]$$
$$= N(t)\alpha_D(t). \tag{C6}$$

To find $\partial n/\partial t|_{\mathrm{DA}}$ we need $\partial f_H(\vec{k})/\partial t|_{\mathrm{DA}}$:

$$\left.\frac{\partial u}{\partial t}\right|_{\mathrm{DA}} = \frac{1}{N_0\hbar\omega_0}\left(\int\frac{2d^3\vec{k}}{(2\pi)^3}E_{c\Gamma}(\vec{k})\left.\frac{\partial f_{c\Gamma}(\vec{k})}{\partial t}\right|_{\mathrm{DA}}\right.$$
$$\left.+2\int\frac{2d^3\vec{k}}{(2\pi)^3}E_H(\vec{k})\left.\frac{\partial f_H(\vec{k})}{\partial t}\right|_{\mathrm{DA}}\right). \tag{16a}$$

Because of the two degenerate valence bands

$$\left.\frac{\partial f_H(\vec{k})}{\partial t}\right|_{\mathrm{DA}} = \frac{1}{2}\left.\frac{\partial f_{c\Gamma}(\vec{k})}{\partial t}\right|_{\mathrm{DA}}. \tag{C7}$$

Thus,

$$\left.\frac{\partial u}{\partial t}\right|_{\mathrm{DA}} = \frac{1}{N_0\hbar\omega_0}\int\frac{2d^3\vec{k}}{(2\pi)^3}[E_{c\Gamma}(\vec{k})+E_H(\vec{k})]\left.\frac{\partial f_{c\Gamma}(\vec{k})}{\partial t}\right|_{\mathrm{DA}}.$$

Because of the δ function $\delta(E_{c\Gamma}(\vec{k})+E_H(\vec{k})-\hbar\omega_0)$ in $\partial f_{c\Gamma}(\vec{k})/\partial t\big|_{DA}$, $E_{c\Gamma}(\vec{k})+E_H(\vec{k})=\hbar\omega_0$, and

$$\left.\frac{\partial u}{\partial t}\right|_{DA}=\frac{1}{N_0}\int\frac{2d^3\vec{k}}{(2\pi)^3}\left.\frac{\partial f_{c\Gamma}(\vec{k})}{\partial t}\right|_{DA}=\left.\frac{\partial n}{\partial t}\right|_{DA}=N(t)\alpha_D(t)\,. \tag{27a}$$

(b) *Free-carrier absorptions.* Let us consider the conduction band electrons first. Since the free-carrier absorptions strongly depend on density, and since the density of electrons in the Γ valley is negligible compared to the $L$-$X$ valleys, we will consider the $L$-$X$ valleys only, and ignore the Γ valley.

With the help of the diagrams, like the ones shown in Fig. 9, we find

$$\begin{aligned}
\left.\frac{\partial N_{\lambda\vec{q}}^{(rad)}}{\partial t}\right|_{FCA-EL}=&-\left(\frac{2\pi}{\hbar}\right)\sum_{j\vec{k}}\sum_{\vec{q}'}\sum_{\mu}\left(\frac{2\pi c^2\hbar}{\epsilon_\infty\omega_q}\right)N_{\lambda\vec{q}}^{(rad)}\left(\frac{\hbar}{2\rho\Omega_{\mu q'}}\right)\left(\frac{e}{mc}\right)^2(1+\eta_{\mu q'})\\
&\times f_{cj}(\vec{k})[1-f_{cj}(\vec{k}+\vec{q}-\vec{q}')]\delta(E_{cj}(\vec{k})+\hbar\omega_q-E_{cj}(\vec{k}+\vec{q}-\vec{q}')-\hbar\Omega_{\mu q'})\\
&\times\left|\frac{Q_\mu(\vec{q}')\langle cj,\vec{k}+\vec{q}-\vec{q}'|e^{-i\vec{q}'\cdot\vec{r}}|cj,\vec{k}+\vec{q}\rangle\langle cj,\vec{k}+\vec{q}|e^{i\vec{q}\cdot\vec{r}}\hat{\xi}_\lambda(\vec{q})\cdot\vec{p}|cj,\vec{k}\rangle}{E_{cj}(\vec{k})+\hbar\omega_q-E_{cj}(\vec{k}+\vec{q})}\right.\\
&\quad\left.+\frac{Q_\mu(\vec{q}')\langle cj,\vec{k}-\vec{q}'|e^{-i\vec{q}'\cdot\vec{r}}|cj,\vec{k}\rangle\langle cj,\vec{k}+\vec{q}-\vec{q}'|e^{i\vec{q}\cdot\vec{r}}\hat{\xi}_\lambda(\vec{q})\cdot\vec{p}|cj,\vec{k}-\vec{q}'\rangle}{E_{cj}(\vec{k}+\vec{q}-\vec{q}')-E_{cj}(\vec{k}-\vec{q}')-\hbar\omega_q}\right|^2\\
&-\left(\frac{2\pi}{\hbar}\right)\sum_{j\vec{k}}\sum_{\vec{q}'}\sum_{\mu}\left(\frac{2\pi c^2\hbar}{\epsilon_\infty\omega_q}\right)N_{\lambda\vec{q}}^{(rad)}\left(\frac{\hbar}{2\rho\Omega_{\mu q'}}\right)\left(\frac{e}{mc}\right)^2\eta_{\mu q'}\\
&\times f_{cj}(\vec{k})[1-f_{cj}(\vec{k}+\vec{q}+\vec{q}')]\delta(E_{cj}(\vec{k})+\hbar\omega_q-E_{cj}(\vec{k}+\vec{q}+\vec{q}')+\hbar\Omega_{\mu q'})\\
&\times\left|\frac{Q_\mu(\vec{q}')\langle cj,\vec{k}+\vec{q}+\vec{q}'|e^{i\vec{q}'\cdot\vec{r}}|cj,\vec{k}+\vec{q}\rangle\langle cj,\vec{k}+\vec{q}|e^{i\vec{q}\cdot\vec{r}}\hat{\xi}_\lambda(\vec{q})\cdot\vec{p}|cj,\vec{k}\rangle}{E_{cj}(\vec{k})+\hbar\omega_q-E_{cj}(\vec{k}+\vec{q})}\right.\\
&\quad\left.+\frac{Q_\mu(\vec{q}')\langle cj,\vec{k}+\vec{q}'|e^{i\vec{q}'\cdot\vec{r}}|cj,\vec{k}\rangle\langle cj,\vec{k}+\vec{q}+\vec{q}'|e^{i\vec{q}\cdot\vec{r}}\hat{\xi}_\lambda(\vec{q})\cdot\vec{p}|cj,\vec{k}+\vec{q}'\rangle}{E_{cj}(\vec{k}+\vec{q}+\vec{q}')-E_{cj}(\vec{k}+\vec{q}')-\hbar\omega_q}\right|^2\\
&+\left(\frac{2\pi}{\hbar}\right)\sum_{j\vec{k}}\sum_{\vec{q}'}\sum_{\mu}\left(\frac{2\pi c^2\hbar}{\epsilon_\infty\omega_q}\right)(N_{\lambda\vec{q}}^{(rad)}+1)\left(\frac{\hbar}{2\rho\Omega_{\mu q'}}\right)\left(\frac{e}{mc}\right)^2(1+\eta_{\mu q'})\\
&\times f_{cj}(\vec{k})[1-f_{cj}(\vec{k}-\vec{q}-\vec{q}')]\delta(E_{cj}(\vec{k})-\hbar\omega_q-\hbar\Omega_{\mu q'}-E_{cj}(\vec{k}-\vec{q}-\vec{q}'))\\
&\times\left|\frac{Q_\mu(\vec{q}')\langle cj,\vec{k}-\vec{q}-\vec{q}'|e^{-i\vec{q}'\cdot\vec{r}}|cj,\vec{k}-\vec{q}\rangle\langle cj,\vec{k}-\vec{q}|e^{-i\vec{q}\cdot\vec{r}}\hat{\xi}_\lambda(\vec{q})\cdot\vec{p}|cj,\vec{k}-\vec{q}'\rangle}{E_{cj}(\vec{k})-E_{cj}(\vec{k}-\vec{q})-\hbar\omega_q}\right.\\
&\quad\left.+\frac{Q_\mu(\vec{q}')\langle cj,\vec{k}-\vec{q}'|e^{-i\vec{q}'\cdot\vec{r}}|cj,\vec{k}\rangle\langle cj,\vec{k}-\vec{q}-\vec{q}'|e^{-i\vec{q}\cdot\vec{r}}\hat{\xi}_\lambda(\vec{q})\cdot\vec{p}|cj,\vec{k}-\vec{q}'\rangle}{E_{cj}(\vec{k}-\vec{q}-\vec{q}')+\hbar\omega_q-E_{cj}(\vec{k}-\vec{q}')}\right|^2\\
&+\left(\frac{2\pi}{\hbar}\right)\sum_{j\vec{k}}\sum_{\vec{q}'}\sum_{\mu}\left(\frac{2\pi c^2\hbar}{\epsilon_\infty\omega_q}\right)(N_{\lambda\vec{q}}^{(rad)}+1)\left(\frac{\hbar}{2\rho\Omega_{\mu q'}}\right)\left(\frac{e}{mc}\right)^2\eta_{\mu q'}\\
&\times f_{cj}(\vec{k})[1-f_{cj}(\vec{k}+\vec{q}'-\vec{q})]\delta(E_{cj}(\vec{k})+\hbar\Omega_{\mu q'}-\hbar\omega_q-E_{cj}(\vec{k}+\vec{q}'-\vec{q}))\\
&\times\left|\frac{Q_\mu(\vec{q}')\langle cj,\vec{k}+\vec{q}'-\vec{q}|e^{i\vec{q}'\cdot\vec{r}}|cj,\vec{k}-\vec{q}\rangle\langle cj,\vec{k}-\vec{q}|e^{i\vec{q}\cdot\vec{r}}\hat{\xi}_\lambda(\vec{q})\cdot\vec{p}|cj,\vec{k}\rangle}{E_{cj}(\vec{k})-E_{cj}(\vec{k}-\vec{q})-\hbar\omega_q}\right.\\
&\quad\left.+\frac{Q_\mu(\vec{q}')\langle cj,\vec{k}+\vec{q}'|e^{i\vec{q}'\cdot\vec{r}}|cj,\vec{k}\rangle\langle cj,\vec{k}+\vec{q}'-\vec{q}|e^{-i\vec{q}\cdot\vec{r}}\hat{\xi}_\lambda(\vec{q})\cdot\vec{p}|cj,\vec{k}+\vec{q}'\rangle}{E_{cj}(\vec{k}+\vec{q}'-\vec{q})-E_{cj}(\vec{k}+\vec{q}')+\hbar\omega_q}\right|^2.
\end{aligned}\tag{C8}$$

As before, $j$ refers to the valleys, $\mu$ to the phonon modes. $\Omega_{\mu q'}$ and $\eta_{\mu q'}$ are phonon frequencies and phonon

distributions, respectively. $Q_\mu(\vec{q}')$ are the phonon-electron coupling parameters discussed in the text. We will assume that there are no phonon instabilities, and that

$$\eta_{\mu q'} = \left[\exp\left(\frac{\hbar\Omega_{\mu q'}}{k_B T_L}\right) - 1\right]^{-1} \simeq \frac{k_B T_L}{\hbar\Omega_{\mu q'}}. \tag{C9}$$

As before, the light momenta $q \ll k, q'$ and can be neglected in $f$'s, $\delta$ functions, and the matrix elements. In the $j$th valley, for the Bloch states,[20]

$$\langle cj, \vec{k}+\vec{q} | e^{i\vec{q}\cdot\vec{r}} \hat{\xi}_\lambda(\vec{q})\cdot\vec{p} | cj, \vec{k}\rangle \simeq \langle cj, \vec{k} | \hat{\xi}_\lambda(\vec{q})\cdot\vec{p} | cj, \vec{k}\rangle \simeq \hbar(m/mc)\hat{\xi}_\lambda(\vec{q})\cdot\vec{k}. \tag{C10}$$

Since $q'$ is small compared to the reciprocal-lattice vector[20]

$$\langle cj, k \pm q' | e^{\pm i\vec{q}'\cdot\vec{r}} | cj, k\rangle \simeq 1. \tag{C11}$$

Phonon energies $\hbar\Omega_{\mu q'} \ll E_{cj}$, $\hbar\omega_q$ and can be neglected in the $\delta$ functions. We will also neglect spontaneous photon emission terms, as done before in direct absorptions. With these approximations, and after a redefinition of integration variables, we obtain

$$\left.\frac{\partial N_{\lambda\vec{q}}}{\partial t}\right|_{\text{FCA-EL}} = -\left(\frac{2\pi e^2\hbar}{m_c^2\epsilon_\infty\omega_q^3\rho}\right) N_{\lambda\vec{q}} \sum_j \sum_{\vec{k}} \sum_\mu \sum_{\vec{q}'} \frac{|Q_\mu(\vec{q}')|^2}{\Omega_{\mu q'}} |\hat{\xi}_\lambda(\vec{q})\cdot\vec{q}'|^2 \left(1 + 2\frac{k_B T_L}{\hbar\Omega_{\mu q'}}\right)$$
$$\times [f_{cj}(\vec{k}) - f_{cj}(\vec{k}+\vec{q}')]\,\delta(E_{cj}(\vec{k}) + \hbar\omega_q - E_{cj}(\vec{k}+\vec{q}')). \tag{C12}$$

We again average over light polarization, then perform $(1/N_0)\sum_{\lambda\vec{q}}$, and find

$$\left.\frac{\partial N}{\partial t}\right|_{\text{FCA-EL}} = -N\left(\frac{2\pi^2 e^2\hbar}{3m_c^2\epsilon_\infty\omega_0^3\rho}\right) \sum_j \sum_{\vec{k}} \sum_\mu \sum_{\vec{q}'} \frac{|Q_\mu(\vec{q}')|^2 (q')^2}{\Omega_{\mu q'}} \left(1 + 2\frac{k_B T_L}{\hbar\Omega_{\mu q'}}\right) [f_{cj}(\vec{k}) - f_{cj}(\vec{k}+\vec{q}')]\,\delta(E_{cj}(\vec{k}) + \hbar\omega_0 - E_{cj}(\vec{k}+\vec{q}')). \tag{C13}$$

In our approximate band structure,

$$E_{cL,X}(\vec{k}) = E_G + \hbar^2(\vec{k} - \vec{k}_{L,X})^2/2m_c. \tag{2a}$$

Substituting this in (C13) and summing over the valleys, changing the integration variable $\vec{k}$, we find

$$\left.\frac{\partial N}{\partial t}\right|_{\text{FCA-EL}} = -N\left(\frac{20\pi^2 e^2\hbar}{3m_c^2\epsilon_\infty\omega_0^3\rho}\right) \int \frac{2d^3\vec{k}}{(2\pi^3)} \left[F\left(\frac{E_G + \hbar^2k^2/2m_c - E_F}{k_B T}\right) - F\left(\frac{E_G + \hbar^2k^2/2m_c + \hbar\omega_0 - E_F}{k_B T}\right)\right]$$
$$\times \sum_\mu \int \frac{d^3\vec{q}'}{(2\pi)^3} \frac{|Q_\mu(\vec{q}')|^2 (q')^2}{\Omega_{\mu q'}} \left(1 + 2\frac{k_B T_L}{\hbar\Omega_{\mu q'}}\right) \delta\left(\frac{\hbar^2k^2}{2m_c} + \hbar\omega_0 - \frac{\hbar^2(\vec{k}+\vec{q}')^2}{2m_c}\right), \tag{C14}$$

where $F(x) = (1+e^x)^{-1}$. For optical phonons,

$$\sum_\mu \int \frac{d^3\vec{q}'}{(2\pi)^3} \frac{|Q_\mu(\vec{q}')|^2 (q')^2}{\Omega_{\mu q'}} \left(1 + 2\frac{k_B T_L}{\hbar\Omega_{\mu q'}}\right) \to \left(1 + 2\frac{k_B T_L}{\hbar\Omega_0}\right)\left(\frac{Q_0^2}{\Omega_0}\right) \int \frac{d^3\vec{q}'}{(2\pi)^3} (q')^2.$$

Owing to the $\delta$ function, integration over $\vec{q}'$ is quite simple:

$$\int d^3\vec{q}'\,(q')^2 \delta\left(\frac{\hbar^2k^2}{2m_c} + \hbar\omega_0 - \frac{\hbar^2(\vec{k}+\vec{q}')^2}{2m_c}\right) = \frac{2\pi m_c^3}{\hbar^6 k} \left\{\left[\left(\frac{\hbar^2k^2}{2m_c} + \hbar\omega_0\right)^{1/2} + \left(\frac{\hbar^2k^2}{2m_c}\right)^{1/2}\right]^4 - \left[\left(\frac{\hbar^2k^2}{2m_c} + \hbar\omega_0\right)^{1/2} - \left(\frac{\hbar^2k^2}{2m_c}\right)^{1/2}\right]^4\right\}. \tag{C15}$$

For acoustical phonons, $\Omega_{\mu q'} \simeq c_A q'$ and

$$\sum_{\mu}\int\frac{d^3\vec{q}'}{(2\pi)^3}\frac{|Q_\mu(\vec{q}')|^2(q')^2}{\Omega_{\mu q'}}\left(1+2\frac{k_BT_L}{\hbar\Omega_{\mu q'}}\right)$$

$$-\int\frac{d^3q'}{(2\pi)^3}\frac{(\Lambda_d^2+\frac{2}{3}\Lambda_d\Lambda_u+\frac{1}{3}\Lambda_u^2)}{c_Aq'}(q')^4\left(1+\frac{2k_BT_L}{\hbar c_Aq'}\right)-\frac{1}{(2\pi)^3}\int d^3\vec{q}'\left(\frac{\Lambda^2}{c_A}\right)(q')^3\left(1+\frac{2k_BT_L}{\hbar c_Aq'}\right).$$

One of the integrations is the same as in (C13). The other gives

$$d^3\vec{q}'\,(q')^3\delta\left(\frac{\hbar^2k^2}{2m_c}+\hbar\omega_0-\frac{\hbar^2(\vec{k}+\vec{q}')^2}{2m_c}\right)$$

$$=\left(\frac{2\pi m_c}{5\hbar^2}\right)\left(\frac{2m_c}{\hbar^2}\right)^{5/2}\left\{\left[\left(\frac{\hbar^2k^2}{2m_c}+\hbar\omega_0\right)^{1/2}+\left(\frac{\hbar^2k^2}{2m_c}\right)^{1/2}\right]^5-\left[\left(\frac{\hbar^2k^2}{2m_c}+\hbar\omega_0\right)^{1/2}-\left(\frac{\hbar^2k^2}{2m_c}\right)^{1/2}\right]^5\right\}. \quad \text{(C16)}$$

Substituting (C15) and (C16) in (C14), performing the remaining angular integrations (of $\vec{k}$), then letting $y=\hbar^2k^2/2\hbar\omega_0m_c$, we obtain

$$\left.\frac{\partial N}{\partial t}\right|_{\text{FCA-EL}}=-N\left\{\left[\left(\frac{5e^2m_c^2Q_0^2}{3\epsilon_\infty\rho\pi^2\hbar^4\Omega_0}\right)\left(1+\frac{2k_BT_L}{\hbar\Omega_0}\right)+\left(\frac{10\Lambda^2e^2m_c^2}{3\pi^2c_A^2\epsilon_\infty\rho\hbar^5}\right)(k_BT_L)\right]\int_0^\infty dy\,\{[(y+1)^{1/2}+(y)^{1/2}]^4\right.$$

$$-[(y+1)^{1/2}-(y)^{1/2}]^4\}\left[F\left(\frac{y+\mathcal{E}_G-\epsilon}{\mathcal{T}}\right)-F\left(\frac{y+1+\mathcal{E}_G-\epsilon}{\mathcal{T}}\right)\right]+\left(\frac{e^2\Lambda^2(2m_c)^{5/2}(\hbar\omega_0)^{1/2}}{3\pi^2\epsilon_\infty\rho c_A\hbar^5}\right)$$

$$\left.\times\int_0^\infty dy\,\{[(y+1)^{1/2}+(y)^{1/2}]^5-[(y+1)^{1/2}-(y)^{1/2}]^5\}\left[F\left(\frac{y+\mathcal{E}_G-\epsilon}{\mathcal{T}}\right)-F\left(\frac{y+1+\mathcal{E}_G-\epsilon}{\mathcal{T}}\right)\right]\right\}. \quad \text{(C17)}$$

Thus,

$$\left.\frac{\partial N}{\partial t}\right|_{\text{FCA-EL}}=-N\left[\alpha_1\times5\left(\frac{m_c}{m_h}\right)^2\left(1+2\frac{\omega_0}{\Omega_0}\,\mathcal{T}_L\right)\zeta_0(z_1)+\alpha_2\,\mathcal{T}_L\times5\left(\frac{m_c}{m_h}\right)^2\zeta_0(z_1)+\alpha_3\times5\left(\frac{m_c}{m_h}\right)^{5/2}\zeta_1(z_1)\right]. \quad \text{(C18)}$$

$\partial N/\partial t|_{\text{FCA-HOLES}}$ can be obtained from (C18) by simply omitting $(m_c/m_h)$ factors, replacing $z_1=(\mathcal{E}_G-\epsilon)/\mathcal{T}$ by $z_2=h/\mathcal{T}$, and dividing by 5. Adding electron and hole contributions we obtain $\partial N/\partial t|_{\text{FCA}}$ given by (39).

$\partial u/\partial t|_{\text{FCA}}$ can be obtained by a simple energy-conservation argument:

$$\left.\frac{\partial u}{\partial t}\right|_{\text{FCA}}=\frac{1}{\hbar\omega_0N_0}\left.\frac{\partial U}{\partial t}\right|_{\text{FCA}}=\frac{-1}{\hbar\omega_0N_0}\left.\frac{\partial(\hbar\omega_0N_0N)}{\partial t}\right|_{\text{FCA}}=\alpha_{\text{FCA}}(t)N(t). \quad \text{(C19)}$$

## APPENDIX D: PHONON-ASSISTED RELAXATION

Phonon-assisted relaxation may be represented by the diagrams shown in Fig. 12. Let us consider the $L$-$X$ valley electrons first. Using the electron-phonon coupling Hamiltonian given by (35), we find

$$\left.\frac{\partial f_{cj}(\vec{k})}{\partial t}\right|_{\text{REL}}=\frac{2\pi}{\hbar}\sum_\mu\sum_{\vec{q}'}\frac{|Q_\mu(\vec{q}')|^2\hbar}{2\rho\Omega_{\mu q'}}$$

$$\times\left[(\eta_{\mu q'}+1)\{|\langle cj,\vec{k}|e^{-i\vec{q}'\cdot\vec{r}}|cj,\vec{k}+\vec{q}'\rangle|^2f_{cj}(\vec{k}+\vec{q}')[1-f_{cj}(\vec{k})]\delta(E_{cj}(\vec{k}+\vec{q}')-E_{cj}(\vec{k})-\hbar\Omega_{\mu q'})\right.$$

$$\left.-|\langle cj,\vec{k}-\vec{q}'|e^{-i\vec{q}'\cdot\vec{r}}|cj,\vec{k}\rangle|^2f_{cj}(\vec{k})[1-f_{cj}(\vec{k}-\vec{q}')]\delta(E_{cj}(\vec{k})-E_{cj}(\vec{k}-\vec{q}')-\hbar\Omega_{\mu q'})\}\right.$$

$$+\eta_{\mu q'}\{|\langle cj,\vec{k}|e^{i\vec{q}'\cdot\vec{r}}|cj,\vec{k}-\vec{q}'\rangle|^2f_{cj}(\vec{k}-\vec{q}')[1-f_{cj}(\vec{k})]\delta(E_{cj}(\vec{k})-E_{cj}(\vec{k}-\vec{q}')-\hbar\Omega_{\mu q'})$$

$$\left.-|\langle cj,\vec{k}+\vec{q}'|e^{i\vec{q}'\cdot\vec{r}}|cj,\vec{k}\rangle^2f_{cj}(\vec{k})[1-f_{cj}(\vec{k}+\vec{q}')]\delta(E_{cj}(\vec{k}+\vec{q}')-E_{cj}(\vec{k})-\hbar\Omega_{\mu q'})\}\right]. \quad \text{(D1)}$$

Using (C11), we find

$$\left.\frac{\partial f_{cj}(\vec{k})}{\partial t}\right|_{\mathrm{REL}} = \frac{\pi}{\rho}\sum_{\mu}\sum_{\vec{q}'}\frac{|Q_{\mu}(\vec{q}')|^2}{\Omega_{\mu q'}}\{\eta_{\mu q'}\{[f_{cj}(\vec{k}+\vec{q}')-f_{cj}(\vec{k})]\,\delta(E_{cj}(\vec{k}+\vec{q}')-E_{cj}(\vec{k})-\hbar\Omega_{\mu q'})$$
$$-[f_{cj}(\vec{k})-f_{cj}(\vec{k}-\vec{q}')]\delta(E_{cj}(\vec{k})-E_{cj}(\vec{k}-\vec{q}')-\hbar\Omega_{\mu q'})\}$$
$$+f_{cj}(\vec{k}+\vec{q}')[1-f_{cj}(\vec{k})]\delta(E_{cj}(\vec{k}+\vec{q}')-E_{cj}(\vec{k})-\hbar\Omega_{\mu q'})$$
$$-f_{cj}(\vec{k})[1-f_{cj}(\vec{k})-\vec{q}')]\delta(E_{cj}(\vec{k})-E_{cj}(\vec{k}-\vec{q}')-\hbar\Omega_{\mu q'})]. \tag{D2}$$

We multiply (D2) by $E_{cj}(\vec{k})$ and sum over the electron states and the valleys:

$$\left.\frac{\partial u_e}{\partial t}\right|_{\mathrm{REL}} = \frac{\pi}{\rho N_0\hbar\omega_0}\sum_{j\vec{k}}\sum_{\mu\vec{q}'}\frac{|Q_{\mu}(\vec{q}')|^2}{\Omega_{\mu q'}}[\eta_{\mu q'}E_{cj}(\vec{k})\{[f_{cj}(\vec{k}+\vec{q}')-f_{cj}(\vec{k})]\,\delta(E_{cj}(\vec{k}+\vec{q}')-E_{cj}(\vec{k})-\hbar\Omega_{\mu q'})$$
$$-[f_{cj}(\vec{k})-f_{cj}(\vec{k}-\vec{q}')]\delta(E_{cj}(\vec{k})-E_{cj}(\vec{k}-\vec{q}')-\hbar\Omega_{\mu q'})\}$$
$$+E_{cj}(\vec{k})f_{cj}(\vec{k}+\vec{q}')[1-f_{cj}(\vec{k})]\delta(E_{cj}(\vec{k}+\vec{q}')-E_{cj}(\vec{k})-\hbar\Omega_{\mu q'})$$
$$-E_{cj}(\vec{k})f_{cj}(\vec{k})[1-f_{cj}(\vec{k}-\vec{q}')]\delta(E_{cj}(\vec{k})-E_{cj}(\vec{k}-\vec{q}')-\hbar\Omega_{\mu q'})]. \tag{D3}$$

Using the identities

$$f_{cj}(\vec{k}+\vec{q}')[1-f_{cj}(\vec{k})]\delta(E_{cj}(\vec{k}+\vec{q}')-E_{cj}(\vec{k})-\hbar\Omega_{\mu q'})$$
$$=[(e^{\beta[E_{cj}(\vec{k}+\vec{q}')-E_F]}+1)^{-1}][1-(1+e^{\beta[E_{cj}(\vec{k})-E_F]})^{-1}]\delta(E_{cj}(\vec{k}+\vec{q}')-E_{cj}(\vec{k})-\hbar\Omega_{\mu q'})$$
$$=(e^{\beta(\hbar\Omega_{\mu q'})}-1)^{-1}[(e^{\beta[E_{cj}(\vec{k})-E_F]}+1)^{-1}-(e^{\beta[E_{cj}(\vec{k})+\hbar\Omega_0-E_F]}+1)^{-1}]\delta(E_{cj}(\vec{k}+\vec{q}')-E_{cj}(\vec{k})-\hbar\Omega_{\mu q'})$$
$$=(e^{\beta(\hbar\Omega_{\mu q'})}-1)^{-1}[f_{cj}(\vec{k})-f_{cj}(\vec{k}+\vec{q}')\delta(E_{cj}(\vec{k}+\vec{q}')-E_{cj}(\vec{k})-\hbar\Omega_0), \tag{D4}$$

we find

$$\left.\frac{\partial u_e}{\partial t}\right|_{\mathrm{REL}} = \left(\frac{\pi}{\rho N_0\hbar\omega_0}\right)\sum_{j\vec{k}}\sum_{\mu\vec{q}}\frac{|Q_{\mu}(\vec{q}')|^2}{\Omega_{\mu q'}}\left(\eta_{\mu q'}-\frac{1}{e^{\beta\hbar\Omega_{\mu q'}}-1}\right)$$
$$\times\{E_{cj}(k)[f_{cj}(k+q')-f_{cj}(k)]\,\delta(E_{cj}(k+q')-E_{cj}(k)-\hbar\Omega_{\mu q'})$$
$$-E_{cj}(k)[f_{cj}(k)-f_{cj}(k-q')]\,\delta(E_{cj}(k)-E_{cj}(k-q')-\hbar\Omega_{\mu q'})\}. \tag{D5}$$

Since phonon energies are small,

$$\eta_{\mu q'}-(e^{\beta\hbar\Omega_{\mu q'}}-1)^{-1}\simeq k_BT_L/\hbar\Omega_{\mu q'}-k_BT/\hbar\Omega_{\mu q'}. \tag{D6}$$

Letting $\vec{k}\to\vec{k}+\vec{q}'$ in the second term, we obtain

$$\left.\frac{\partial u_e}{\partial t}\right|_{\mathrm{REL}} = \left(\frac{\pi}{\rho N_0\hbar\omega_0}\right)\sum_{j\vec{k}}\sum_{\mu\vec{q}}\frac{|Q_{\mu}(\vec{q}')|^2}{\Omega_{\mu q'}}\left(\frac{k_BT_L-k_BT}{\hbar\Omega_{\mu q'}}\right)[E_{cj}(\vec{k})-E_{cj}(\vec{k}+\vec{q}')][f_{cj}(\vec{k}+\vec{q}')-f_{cj}(\vec{k})]$$
$$\times\,\delta(E_{cj}(\vec{k}+\vec{q}')-E_{cj}(\vec{k})-\hbar\Omega_{\mu q'}). \tag{D7}$$

Owing to the $\delta$ function,

$$\left.\frac{\partial u_e}{\partial t}\right|_{\mathrm{REL}} = \left(\frac{\pi}{\rho N_0\hbar\omega_0}\right)\sum_{j\vec{k}}\sum_{\mu\vec{q}}\frac{|Q_{\mu}(\vec{q}')|^2}{\Omega_{\mu q'}}(k_BT-k_BT_L)\,[f_{cj}(\vec{k}+\vec{q}')-f_{cj}(\vec{k})]\,\delta(E_{cj}(\vec{k}+\vec{q}')-E_{cj}(\vec{k})-\hbar\Omega_{\mu q'}). \tag{D8}$$

Redefining $\vec{k}$ in each valley, we obtain

$$\left.\frac{\partial u_e}{\partial t}\right|_{\mathrm{REL}} = \frac{10(k_BT-k_BT_L)}{\rho N_0\hbar\omega_0(2\pi)^5}\sum_{\mu}\int d^3\vec{k}\int d^3\vec{q}'\,\frac{|Q_{\mu}(\vec{q}')|}{\Omega_{\mu q'}}$$
$$\times[f(E+E_G+\hbar\Omega_{\mu q'})-f(E+E_G)]\,\delta\left(\frac{\hbar^2kq'\cos\theta}{m_c}+\frac{\hbar^2q'^2}{2m_c}-\hbar\Omega_{\mu q'}\right), \tag{D9}$$

where $\cos\theta = \hat{k}\cdot\hat{q}'$ and

$$E \equiv \hbar^2 k^2/2m_c\,, \quad f(E) \equiv (e^{\beta(E-E_F)}+1)^{-1}\,. \tag{D10}$$

Since phonon energies are small,

$$f(E+E_G+\hbar\Omega_{\mu q'})-f(E+E_G) \simeq \hbar\Omega_{\mu q'}\left(\frac{\partial f(E+E_G)}{\partial E}\right) \tag{D11}$$

and $\hbar\Omega_{\mu q'}$ can be omitted from the $\delta$ function. Thus,

$$\left.\frac{\partial u_e}{\partial t}\right|_{\rm REL} = \frac{10(k_BT-k_BT_L)}{\rho N_0\omega_0(2\pi)^5}\sum_\mu \int d^3\vec{k}' \int d^3\vec{q}'\,|Q_\mu(\vec{q}')|^2 \frac{\partial f(E+E_G)}{\partial E}\,\delta\left(\frac{\hbar^2 kq'\cos\theta}{m_c}+\frac{\hbar^2 q'^2}{2m_c}\right). \tag{D12}$$

Substituting the properly angular averaged electron-phonon coupling coefficients we find

$$\left.\frac{\partial u_e}{\partial t}\right|_{\rm REL} = \frac{10(k_BT-k_BT_L)}{\rho N_0\omega_0(2\pi)^5}\int d^3\vec{k}' \int d^3\vec{q}'\,(Q_0^2+\Lambda^2 q'^2)\frac{\partial f(E+E_G)}{\partial E}\,\delta\left(\frac{h^2 kq'\cos\theta}{m_c}+\frac{\hbar^2 q'^2}{2m_c}\right). \tag{D13}$$

The remaining integrals are trivial, and we find (in terms of the normalized quantities)

$$\left.\frac{\partial u_e}{\partial t}\right|_{\rm REL} = -\Gamma^{(0)}5\left(\frac{m_c}{m_h}\right)^3 \mathcal{T}(\mathcal{T}-\mathcal{T}_L)\ln(1+e^{-z_1}) - \Gamma^{(a)}5\left(\frac{m_c}{m_h}\right)^4 \mathcal{T}^2(\mathcal{T}-\mathcal{T}_L)\kappa(z_1)\,. \tag{D14}$$

$\partial u_h/\partial t\,|_{\rm REL}$ can be obtained from (D14) by replacing $z_1$ by $z_2$, dividing by 5, and omitting $(m_c/m_h)$ factors.

## APPENDIX E: EXPERIMENTAL METHOD AND DETAILS

(a) *Introduction.* This appendix contains an elaboration of the experimental method. This presentation of the experimental apparatus is given in detail because picosecond pulse techniques are not a standard tool of solid-state physicists, and some aspects of sample preparation may be of interest to the "nonsolid staters." The first experimental section contains a description of the mode-locked Nd:glass laser system, electro-optical switch-out apparatus, and the pulse splitter and delay optics. The second section presents properties of the germanium sample, including purity, surface preparation, and thickness measurement. The third section discusses the detection system, and the fourth discusses possible sources of experimental error. Figure 31 shows the entire apparatus in block diagram form.

(b) *Pulse preparation.* The production of very short optical pulses by mode-locking requires a laser system with an active medium that provides a large gain bandwidth for light amplification. $Nd^{3+}$:glass, with a fluorescent bandwidth of 2.7 $\times 10^{12}$ Hz, has the potential of producing pulses as short as 0.3 psec. In practice, pulses between 5 and 15 psec duration are obtained. This deviation from the theoretically calculated pulse width is caused by the broadening of short pulses in a dispersive and nonlinear medium and by spectral narrowing due to preferential amplification of frequency components close to the gain maximum. In fact, pulse widths would be wider than those observed if it were not for the pulse shortening effects of the nonlinear saturable absorber that is used to passively mode lock the laser. For a discussion of the basic principles of mode-locking and the production of ultrashort laser pulses, the reader is referred to von der Linde.[1]

The mode-locked output from the Nd:glass laser system employed in these experiments consists of a series of approximately 100 pulses separated one from the next by approximately 8 nsec. Each pulse is typically 5–10 psec in duration and has an energy of 0.1 mJ at a wavelength of 1.06 $\mu$m. The laser produces single well mode-locked pulse trains on more than 80% of its firings. A brief description of the laser hardware follows.

The active lasing medium, a Brewster-cut Owens-Illinois ED-2S Nd:glass rod approximately 19 cm long and 6.4 mm in diameter, is housed in a Korad K1 laser head. The glass rod is pumped by a helical xenon flash lamp with an arc length of 28 in. A high-voltage, symmetrically shaped pulse

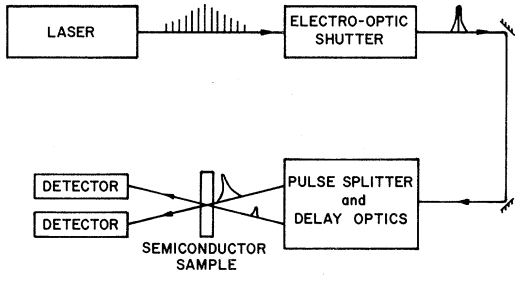


FIG. 31. Block diagram of the experiment.

from a 10-kV power supply is used to ionize the xenon gas. The high-voltage pulse is 0.5 msec in duration, and it typically delivers an energy of 600 J at 4.5 kV. Both flash lamp and glass rod are cooled by circulating water maintained at room temperature. The power supply consists of a 60-$\mu$F capacitor bank plus pulse shaping electronics. The flash lamp and power supply are fired approximately once per minute.

The laser oscillator cavity is 120 cm long with a spherical mirror of radius 2.5 m with a reflectivity of 99.7% at 1.06 $\mu$m at one end and a flat mirror with a reflectivity of 27% at the output end. The laser is mode-locked by placing a 1-mm-thick cell containing at 10:1 solution of dichloroethane and Eastman $Q$-switch solution A9860 in contact with the output mirror. The output mirror forms one face of the dye cell. Thus it must be resistant to the solvent dichloroethane as well as withstand the high-power levels of the optical pulses. The mode-locking dye is replenished after each laser firing by siphoning fresh dye solution from a reservior with a hypodermic needle.

The single most critical component of the entire laser system is the glass laser rod. Self-focusing of the pulse propagating in the glass rod, due to the nonlinear refractive index $n_2$, is a major problem in achieving reliable mode-locking in this laser. Using Owens-Illinois type ED-2S laser glass, we obtained clean pulse trains on approximately 80% of the firings.

In order to perform the two experiments, a single pulse must be selected from the train of picosecond pulses. Figure 32 shows the electro-optical shutter used to perform this function. The pulse train passes through a Pockels cell placed between two Glan prisms which act as nonabsorbing crossed polarizers. If no voltage is applied to the Pockels cell, the light passes through with no change in polarization and is rejected by the second crossed polarizer. When the half wave voltage is applied to the Pockels cell, the light polarization is rotated by 90° and thus the light is transmitted by the second polarizer. Voltage is held off the Pockels cell until

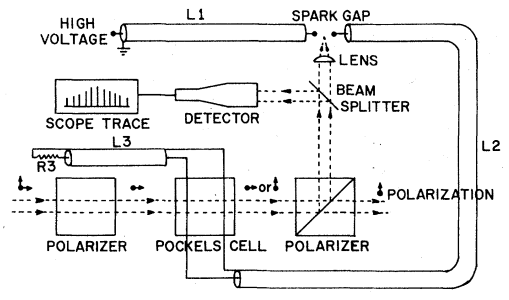


FIG. 32. Electro-optical shutter.

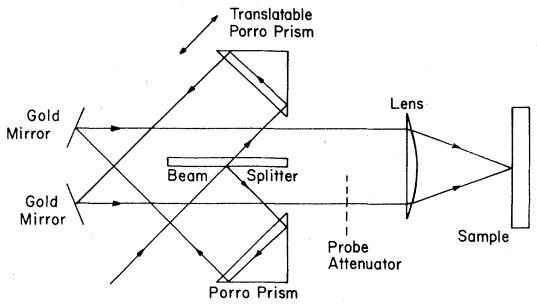


FIG. 33. Pulse splitter and delay optics.

the first part of the pulse train, which is reflected by the second Glan prism, breaks down a spark gap. Upon breakdown, a voltage pulse from a charged transmission line is applied to the Pockels cell; the length of the charged line is chosen such that the duration of the voltage pulse is equal to the temporal pulse separation in the train in order that one and only one pulse is switched out of the train.

In order to perform the two pulse or probe experiments, the single pulse selected from the train must be split in two and a variable delay must be introduced between these two pulses. Figure 33 is a detail of the pulse splitter and delay optics. Although a weak probe pulse is generally desired for the probe experiment, the pulse is split by a 50-50 beam splitter for ease in alignment of the two pulses coincident on the sample surface. The variable optical delay is introduced by means of a translatable Porro prism. The plano-convex lens, focal length $f = 20$ cm, serves to increase the optical energy density of the pulse and to angularly separate the two pulses for detection. The lens is placed after the pulse splitter and delay optics in order that the probe pulse spot size in the plane of the sample remains independent of the prism position. Alignment of the optical components and translation of the prism are critical in order that the two pulses are spatially coincident on the plane of the sample and remain that way during the experiment. Alignment of the two pulses is confirmed by inspection of burn patterns on exposed Polaroid film placed in the plane of the sample, because the red beams used for alignment of the laser are not coincident with the infrared laser output after passing through all the switch-out and pulse splitter and delay optics.

(c) *Crystal sample.* The semiconductor material used in these experiments is intrinsic germanium. The minimum resistivity of the high-purity single crystal sample is 40.0 Ω cm at room temperature. The sample was prepared from a crystal wafer 1 in. in diameter. First one surface was polished flat and smooth and then etched with Syton. The purpose of etching is to remove the damaged (from

mechanical polishing) surface layer and clean the surface of impurities in order that the optical measurements reflect the bulk properties of the solid. As is well known, etching the sample surface has an important effect on the observation of recombination radiation of germanium excited by a thermal source. After the first surface was prepared, the sample was bonded to a KZF-2 glass substrate, which has approximately the same coefficient of thermal expansion as germanium and is transparent at the laser wavelength. Then the sample was ground down to the desired thickness and the second surface was also polished and etched. Sample thickness is determined to be 5.2 $\mu$m by the interference fringe spacing of the reflection spectra measured in the infrared region of 3–15 $\mu$m. Crystallinity of the sample is verified by observing the x-ray diffraction pattern of the sample. During the measurements the sample on the substrate is mounted in an evacuated Dewar with quartz windows in order that the sample can be cooled. The sample temperature is measured by a thermocouple in contact with the crystal surface.

(d) *Detection system.* Two different types of detectors are used in these experiments. The entire pulse train (minus the switched out pulse) is monitored in order to verify that the pulse train is well mode-locked. To do this, the laser output is displayed on an ITT model F4000 biplanar vacuum photodiode and a Tektronix model 519 oscilloscope; the combined response time is approximately 1 nsec.

The primary measurement in these experiments is the measurement of energy in a single (incident, reflected, or transmitted) picosecond pulse. This is done by means of United Detector Technology model 6D silicon *p-i-n* photodiode operated in the photoconductive mode. When the laser pulse is incident on the large area photodiode, electron-hole pairs created in the intrinsic region junction are swept out by the reverse bias and charge an integrating capacitor. The voltage on this capacitor is proportional to the energy in the pulse and is read by means of a peak-detector-and-hold circuit and displayed on a digital voltmeter. The optical collection system is designed such that the detectors intercept radiation only from a small solid angle completely filled by the sample. Electrical shielding reduces pickup of electrical noise from the flash discharge. Detection of recombination radiation from germanium is eliminated by the sharp cutoff in spectral sensitivity of the silicon photodiodes at 1.1 $\mu$m.

The pulse energy detectors were calibrated both absolutely and relatively. Absolute calibration was performed against a calibrated Quantronix model 500 energy receiver and model 504 energy/power meter. Relative sensitivities of the detector units were measured with the units placed in their respective experimental configurations.

(e) *Experimental error.* We believe the main sources of error for both excitation and excitation-probe measurements to be the variation in pulse width and in energy from one laser firing to the next. The laser pulse train envelope is somewhat irreproducible, and the pulse width and shape vary with the location of the pulse in the train of pulses, as described by von der Linde.[1] This irreproducible and random nature of the pulse evolution within the laser cavity precludes the continued selection of identical pulses by the laser-triggered spark gap. The pulse width (unmeasured) is believed to range from 5 to 10 psec in duration. The dependence of the excitation-probe data on the level of excitation is clearly depicted in Fig. 4; the theoretical dependence of the single pulse (excitation transmission data on pulse width are illustrated in Fig. 25).

In addition to the uncertainty in pulse energy and width from data point to data point, the transverse mode structure of the laser is also uncertain (uncontrolled). Deviations of the transverse mode structure from the $TEM_{00}$ mode will lead to "hot" spots on the surface of the semiconductor sample when the beam is focused. Variations in the positions of these "hot" spots as the mode structure changes from one firing to the next will result in variations in the degree of overlap between the excitation and probe beams and consequently will result in scatter in the probe transmission.

---

*During the course of this work we have appreciated the support of the ERDA, the NSF, the Alfred P. Sloan Foundation, the U. S. Air Force, (SAMSO), the Office of Naval Research, and the Al-Hazen Research Institute (Baghdad, Iraq).

[1]D. von der Linde, Appl. Phys. 2, 281 (1973).
[2]J. W. Shelton and J. A. Armstrong, IEEE J. Quantum Electron. QE-3, 696 (1967).
[3]C. J. Kennedy, J. C. Matter, A. L. Smirl, H. Weichel, F. A. Hopf, and S. V. Pappu, Phys. Rev. Lett. 32, 419 (1974).
[4]D. H. Auston and C. V. Shank, Phys. Rev. Lett. 32, 1120 (1974).
[5]A. L. Smirl, J. C. Matter, A. Elci, and M. O. Scully, Opt. Commun. 16, 118 (1976).
[6]D. von der Linde, O. Bernechker, and A. Laubereau, Opt. Commun. 2, 215 (1970).
[7]W. C. Dash and R. Newman, Phys. Rev. 99, 1151

(1955).
[8]H. Shih, M. Scully, W. H. Louisell, and W. B. McKnight, Appl. Opt. 12, 2198 (1973).
[9]M. Neuberger, *Handbook of Electronic Materials* (Plenum, New York, 1971), Vol. 5.
[10]Since the minima of the $L$ valleys are exactly at the Brillouin-zone boundary, there are four of them instead of eight. But the minima of the valleys along $\Delta_1$ are at $k \simeq 0.8kX$; therefore, there are six of them.
[11]Density-of-states effective mass is defined as $(m_t^2 m_l)^{1/3}$, where $m_t$ and $m_l$ are transverse and longitudinal effective masses, respectively.
[12]Indirect transitions are discussed in J. Bardeen, F. J. Blatt and L. H. Hall, in *Proceedings of the Conference on Photoconductivity, Atlantic City, November 4—6,* edited by R. G. Breckneridge *et al.* (Wiley, New York, 1956).
[13]A few notational comments: the tilda on a summation sign means that the summation is divided by the normalization density $N_0$. Electron or hole spin summations are not shown explicitly, but should be understood. The script letters denote the normalized quantities, and the corresponding ordinary type letters denote the corresponding unnormalized quantities in ordinary units (cgs).
[14]H. Y. Fan, M. L. Shepherd, and W. Spitzer, in Ref. 12.
[15]D. L. Dexter, in Ref. 12.
[16]A. H. Kahn, Phys. Rev. 97, 1647 (1955).
[17]H. Y. Fan, W. Spitzer, and R. J. Collins, Phys. Rev. 101, 566 (1956).
[18]R. Rosenberg and M. Lax, Phys. Rev. 112, 843 (1958).
[19]M. Lax and J. J. Hopfield, Phys. Rev. 124, 115 (1961).
[20]H. J. G. Meyer, Phys. Rev. 112, 298 (1958); J. Phys. Chem. Solids 8, 264 (1959).
[21]J. M. Lutthinger and W. Kohn, Phys. Rev. 97, 869 (1955).
[22]If there were no valleys, this statement would not be true. In that case the free-carrier absorptions could become dominant at high light intensities.
[23]C. A. Hogarth, in *Materials Used in Semiconductor Devices*, edited by C. A. Hogarth (Interscience, New York, 1965).
[24]Walter A. Harrison, Phys. Rev. 104, 1281 (1956).
[25]C. Herring and E. Vogt, Phys. Rev. 101, 944 (1956).
[26]B. N. Brockhouse and P. K. Iyengar, Phys. Rev. 111, 747 (1958).
[27]C. Herring, Bell Syst. Tech. J. 34, 237 (1955).
[28]$c_L = 2.31$ for Ge.
[29]P. A. Wolff, Phys. Rev. Lett. 24, 266 (1970).
[30]P. Nozières and D. Pines, Phys. Rev. 109, 741 (1958).
[31]J. J. Quinn and R. A. Ferrell, Phys. Rev. 112, 812 (1958).
[32]The portion of the incident pulse intensity that is reflected from the front surface must be subtracted from the incident pulse intensity to obtain the source term.
[33]The loss term takes into account the internal reflection from the rear surface of the crystal, which decreases transmission.
[34]The maximum refractive index change observed is $\Delta n/n \simeq -0.05$ (see Ref. 4).
[35]In the initial phase, practically all photons that are absorbed are used in increasing the electron density. Also, at this stage, the electron density is quite small, and therefore the high-temperature approximation can be made to calculate the electron and hole energy density. This energy density is then given by $nN_0(E_G + \frac{3}{2}k_BT) + nN_0 \times \frac{3}{2}k_BT$. Setting this equal to the radiation energy density that is absorbed, $nN_0\hbar\omega_0$, we find $k_BT = \frac{1}{3}(\hbar\omega_0 - E_G)$, or in terms of the normalized quantities, $\mathcal{T} = \frac{1}{3}(1 - \mathcal{E}_G)$.
[36]The authors would like to comment at this point that the absolute values of the probe transmissions shown in these figures are higher than those experimentally observed. This is a result of the approximations made in describing the Ge band structure. Further study has shown that the absolute transmission may be adjusted by removing some of these approximations. These points are discussed in a following paper.
[37]The refractive index for the optical frequency $\omega_0$ is approximately given by $[\epsilon_\infty(1 - \omega_p^2/\omega_0^2)]^{1/2}$.